A comparative study of different mesh types for transport processes near gas bubbles regarding accuracy, stability, and run time

Eine Vergleichsstudie verschiedener Netztypen für die Simulation von Transportvorgängen um Gasblasen bezüglich Genauigkeit, Stabilität und Rechenzeit

Bachelor-Thesis von Jan-Alexander Kleikemper

Tag der Einreichung:

1. Gutachten: Prof. Dr. Dieter Bothe
2. Gutachten: Prof. Dr.-Ing. Cameron Tropea

TECHNISCHE UNIVERSITÄT DARMSTADT

Mathematical Modeling and Analysis

A comparative study of different mesh types for transport processes near gas bubbles regarding accuracy, stability, and run time

Eine Vergleichsstudie verschiedener Netztypen für die Simulation von Transportvorgängen um Gasblasen bezüglich Genauigkeit, Stabilität und Rechenzeit

Vorgelegte Bachelor-Thesis von Jan-Alexander Kleikemper

1. Gutachten: Prof. Dr. Dieter Bothe
2. Gutachten: Prof. Dr.-Ing. Cameron Tropea

Tag der Einreichung:

Erklärung zur Bachelor-Thesis

Hiermit versichere ich, die vorliegende Bachelor-Thesis ohne Hilfe Dritter nur mit den angegebenen Quellen und Hilfsmitteln angefertigt zu haben. Alle Stellen, die aus Quellen entnommen wurden, sind als solche kenntlich gemacht. Diese Arbeit hat in gleicher oder ähnlicher Form noch keiner Prüfungsbehörde vorgelegen.

Darmstadt, den 4. April 2018

_____

(Jan-Alexander Kleikemper)

Abstract

Mass transfer at a single gas bubble rising in incompressible liquid is studied. Only the liquid phase is simulated. A fixed bubble model is used and non-deformable spheroidal gas bubbles with aspect ratio $\chi = 3$ are considered. The Reynolds number is varied between 50 and 500 and two Schmidt numbers, 10 and 100, are taken into account. Four meshing strategies are compared with respect to accuracy, stability and run-time. The main focus is on mesh sensitivity of the target quantities close to the interface and in the bubble wake. The results are compiled in a Best Practice Guide.

Stofftransfer an einer einzelnen aufsteigenden Gasblase in inkompressibler Flüssigkeit wird untersucht. Nur die Flüssigphase wird simuliert. Ein statisches Blasenmodell wird verwendet und Sphäroide mit Seitenverhältnis $\chi = 3$ werden untersucht. Die Reynoldszahl wird zwischen 500 and 50 variiert und zwei Schmidtzahlen, 100 and 10, werden berücksichtigt. Vier Vernetzungsstrategien werden verglichen mit Blick auf Genauigkeit, Stabilität und Rechenzeit. Der Hauptfokus liegt auf Netzsensitivität der Zielgrößen um die Blasenoberfläche und im Nachlauf der Blase. Die Ergebnisse sind in einem „Best Practice Guide“ zusammengetragen.

Contents

List of Tables

List of Figures

Nomenclature

Dimensionless Groups

Co	Courant number	$U\Delta t/\Delta x$
Eo	Eötvös number	$\Delta\rho g d_b^2/\sigma$
Mo	Morton number	$g\mu_l^4\Delta\rho/\rho_l^3\sigma^3$
Pe	Peclet number	$Re \cdot Sc = U_b d_b/D$
Re	Reynolds number	$U_b d_b/\nu$
Sc	Schmidt number	ν/D
Sh	Sherwood number	$k_a d_b/D$

Roman Symbols

A	transfer species	
a	semi-major axis of the bubble	[mm]
b	semi-minor axis of the bubble	[mm]
c	concentration of species A	$[\mathrm{mol\,m^{-3}}]$
D	Diffusitivity	$[\mathrm{m^2\,s^{-1}}]$
d_b	equialent bubble diameter	[mm]
g	gravitation constant	$9.81\,\mathrm{m\,s^{-2}}$
k_a	mass transfer coefficient	$[\mathrm{m\,s^{-1}}]$
p	pressure	$[\mathrm{kg\,m^{-1}\,s^{-2}}]$
r	radius	[mm]
T	temperature	[°C]
t	time	[s]
$\underline{u}$	velocity vector	$[\mathrm{m\,s^{-1}}]$
U_b	rise velocity of the bubble	$[\mathrm{m\,s^{-1}}]$

Greek Symbols

δ_c	concentration boundary layer	[μm]
δ_h	hydrodynamic boundary layer	[μm]
η	dynamic viscosity	$[\mathrm{kg\,m^{-1}\,s^{-1}}]$
ν	kinematic viscosity	η/ρ $[\mathrm{m^2\,s^{-1}}]$

π	circle's circumference to its diameter	3.1415
ρ	density	$[\mathrm{kg\,m^{-3}}]$
σ	surface tension coefficient	$[\mathrm{kg\,s^{-2}}]$
$\underline{\underline{\tau}}$	shear stress tensor	$[\mathrm{N\,m^{-2}}]$
φ	scale of segregation	$[\mathrm{m^{-1}}]$
χ	aspect ratio	[]

Subscripts

b	bubble	
eq	equivalent	used for the Sherwood numbers that are normalized with the area of a sphere with equivalent volume and the equivalent bubble diameter
in	inlet	as in inlet velocity U_{in}
l	liquid	
loc	local	as in local Sherwood number Sh_{loc}
o	outer sphere	

Superscripts

T	transpose	

1 Introduction

Species transfer between gaseous and liquid phases has an enormous influence and relevance for industrial processes. Bubble column reactors, for example, play an important role in pharmaceutical, agrochemical and dye-manufacturing industries. Some frequently cited advantages of gas-liquid reactors are good heat and mass transfer characteristics and low maintenance and operation costs [3, 6].

To simulate entire bubble column reactors, Euler-Euler and Euler-Lagrange simulations are used, since currently available computing capabilities do not allow direct numerical simulations (DNS) of hydrodynamics and chemical reactions of the whole reactor. This is because of the wide range of relevant length scales ranging from the reactor size down to the Batchelor scale, which determines the smallest structures of species transport in turbulent flows. In scale-reduced approaches, the influence of the small scales is modelled. In turn, for reliable models of small scales, investigations on the scale of single bubbles are required, which is the starting point for the present work.

In bubble column reactors, bubbles occur in different shapes and the shape of a single bubble changes on its way through the column. To simplify the problem, no dynamic variation of the shape is considered. In [5] a shape regime diagram (Figure 1.1a) is presented that shows different bubble shapes dependent on three dimensionless groups.

The Reynolds number Re is an important dimensionless number in fluid dynamics. It describes the ratio between inertial and viscous forces and is typically defined as

$$Re = \frac{UL}{\nu} = \frac{U_b d_{eq}}{\nu_l}, \tag{1.1}$$

where U is the velocity of the fluid relative to the object, in this case the bubble rise velocity U_b; L is the characteristic length, for bubbles the equivalent bubble diameter d_{eq}; ν the kinematic viscosity, here of the liquid phase ν_l.

The Eötvös number Eo (also referred to as Bond number Bo), together with the Morton number, is an important indicator in fluid dynamics to characterize the shape of bubbles in the surrounding liquid. It relates the impact of gravitational forces and surface tension forces on the bubble and it is defined as

$$Eo = Bo = \frac{\Delta\rho g L^2}{\sigma}. \tag{1.2}$$

Here, g is the graviation constant, $\Delta\rho$ is the density difference of the phases $\rho_l - \rho_g$, σ is the surface tension coefficient and L is the characteristic length as in (1.1).

The Morton number Mo measures the relation of viscous and surface forces in two-phase flows. It is a function of the material properties of both gas and liquid phases and it reads as

$$Mo = \frac{g\,\nu_l^4 \Delta\rho}{\rho_l^3 \sigma^3} \tag{1.3}$$

with ν_l being the dynamic viscosity of the liquid phase, ρ_l the density of the liquid phase and g, $\Delta\rho$ and σ as defined for (1.2).

The diagram 1.1a suggests that bubbles with a spherical or spheroidal shape occur in the ranges of $Re \leq 1000$,

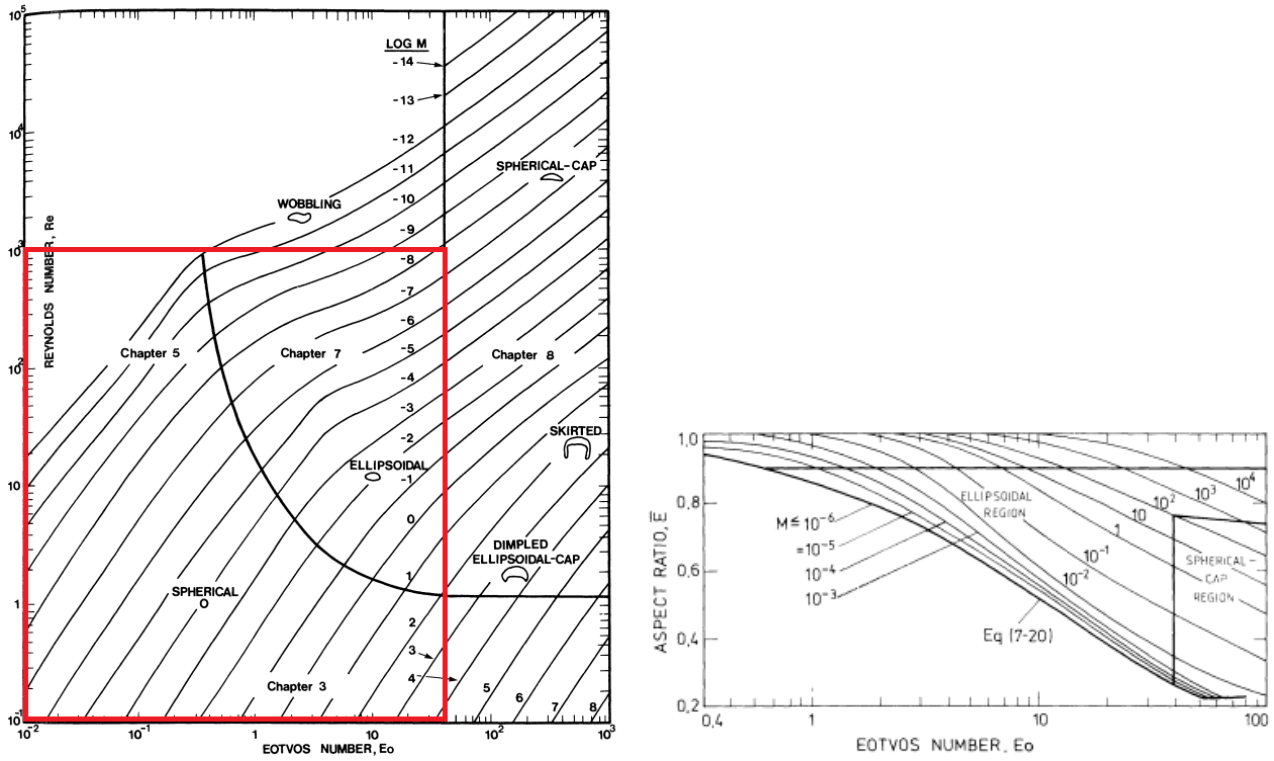

(a) Re-Eo-Mo diagram

(b) Eo-χ diagram

Figure 1.1: Re-Eo-Mo and Eo-χ diagrams, figures reproduced from [5].

$Eo \leq 40$ and $\log(Mo) \geq -12$. The second diagram (Figure 1.1b), from [5], asserts that in the range of $Eo \leq 40$ eccentrities up to $E \approx 0.25$ occur, depending on the Morton numbers that lie above the limit of $log(Mo) \geq -12$. In the present work, the shape of the bubble is defined by the aspect ratio χ[1], which is reciprocal to the eccentrity E. A similar approach was taken in [4].

The Schmidt number Sc is used to describe the ratio between viscous and molecular diffusion:

$$Sc = \frac{\nu_l}{D}, \tag{1.4}$$

with the mass diffusitivity of the species D and the kinematic viscosity of the liquid phase ν_l. Typical Schmidt numbers for common gases diluted in water (kinematic viscosity $\nu_l = 8.917 \cdot 10^{-7}\,\mathrm{m^2\,s^{-1}}$, $T = 25\,^{\circ}\mathrm{C}$) are listed in Table 1.1.

Dissolved gas	Molecular diffusitivity D [$\mathrm{m^2\,s^{-1}}$]	Sc for $\nu = 8.917 \cdot 10^{-7}\,\mathrm{m^2\,s^{-1}}$
N_2	$1.88 \cdot 10^{-9}$	474
O_2	$2.10 \cdot 10^{-9}$	425
CO_2	$1.92 \cdot 10^{-9}$	464
H_2	$4.50 \cdot 10^{-9}$	198
Air	$2.00 \cdot 10^{-9}$	446

Table 1.1: Typical Schmidt numbers at 25 °C.

[1] A definition of the aspect ratio follows in chapter 2.

Two boundary layers are present around the bubble: the hydrodynamic boundary layer δ_h and the concentration boundary layer δ_c. The Schmidt number can be interpreted as a measure for the ratio between the hydrodynamic and the concentration boundary layer (δ_h/δ_c). For most gases that are dissolved in water, the kinematic viscosity ν is large compared to the diffusitivity D. This leads to Schmidt numbers $\gg 1$, which means that the concentration boundary layer δ_c is thin compared to the hydrodynamic boundary layer δ_h, see [6]. Therefore, in numerical simulations it is reasonable to assume that the hydrodynamic boundary layer δ_h is resolved if the concentration boundary layer δ_c is so.

To get a first idea about the required mesh resolution close to the bubble, it is useful to estimate the boundary layer thicknesses based on simplifying theories like potential flow and film theory. For that, two dimensionless groups are introduced, the Peclet and the Sherwood number.

The Peclet number Pe is the product of Reynolds and Schmidt number, i.e. it defines the ratio between convective and diffusive transport,

$$Pe = Re \cdot Sc = \frac{U_b d_b}{\nu} \frac{\nu}{D} = \frac{U_b d_b}{D}. \tag{1.5}$$

The Sherwood number is a dimensionless measure for the concentration gradient at the interface. It can be described as a function of the mass transfer coefficient k_a,

$$Sh = \frac{k_a d_b}{D}. \tag{1.6}$$

Using potential flow theory and a thin concentration layer approximation, Sherwood and Peclet numbers can be related as $Sh = 2 \cdot \sqrt{Pe}/\sqrt{\pi}$, see [6].
Moreover, using film theory, δ_c can be approximated as $\delta_c = d_b/Sh$. This leads to the following approximation for δ_c:

$$\delta_c = d_b \cdot \frac{\sqrt{\pi}}{2} \cdot \frac{1}{\sqrt{Pe}}. \tag{1.7}$$

For a bubble of $d_b = 2\,\text{mm}$ and a flow characterized by $Re = 500$ and $Sc = 100$ the average concentration boundary layer is $\delta_c = 8\,\mu\text{m}$. To resolve the steep concentration gradients, at least five cell layers should lie in the boundary layer, see [4, p.6299]. The estimated concentration boundary layer thickness would then require cell thicknesses of $8\,\mu\text{m}/5 = 1.6\,\mu\text{m}$.
With the intervals of Re [5;500] and Sc [10;100] taken into account, the interval of Pe is $5 \cdot 10^2$ to $1 \cdot 10^5$. The estimated concentration boundary layer thicknesses for the occurring Peclet numbers are listed in Table 1.2. Note that the estimates in Table 1.2 are more accurate for higher Reynolds numbers.

	$Re = 5$	$Re = 50$	$Re = 500$
$Sc = 10$	$250\,\mu\text{m}$	$79\,\mu\text{m}$	$25\,\mu\text{m}$
$Sc = 100$	$79\,\mu\text{m}$	$25\,\mu\text{m}$	$7.9\,\mu\text{m}$

Table 1.2: Estimated concentration boundary layer thicknesses for different Peclet numbers.

The goal of this work is to evaluate meshing strategies that allow efficient numerical simulations of species transport near a single bubble. The meshes are compared with regard to accuracy, stability and run time of the simulation.
One criterion to evaluate the quality of a computation is mesh (in)dependency. Unfortunately, a finer mesh leads to

higher computational costs. Thus, it is essential to identify where the mesh has to be the finest and where fewer cells are sufficient. In fact, the required cell number depends on the presence and magnitude of gradients of pressure, velocity and species concentration. In the boundary layer around the bubble and in its vicinity and in the wake of the bubble, the gradients are strongest, which requires the highest mesh resolution to be in these areas. One focus of this work is to evaluate different meshing strategies in order to control the resolution in certain areas of the mesh.

Due to the very demanding mesh resolutions, Reynolds numbers up to 500 and Schmidt numbers equal to 10 and 100 are considered. To further reduce the complexity of the simulations, only the flow around fixed bodies of revolution is considered, although in real bubble column reactors the shape of the bubbles is varying.
Figure 1.2 from [4] suggests that for $Re = 500$ and $\chi = 3$ three-dimensional flow patterns with an unsteady wake are expected. Because those flow patterns are the most demanding in terms of mesh resolution, this setup is used for the study of the mesh dependency.

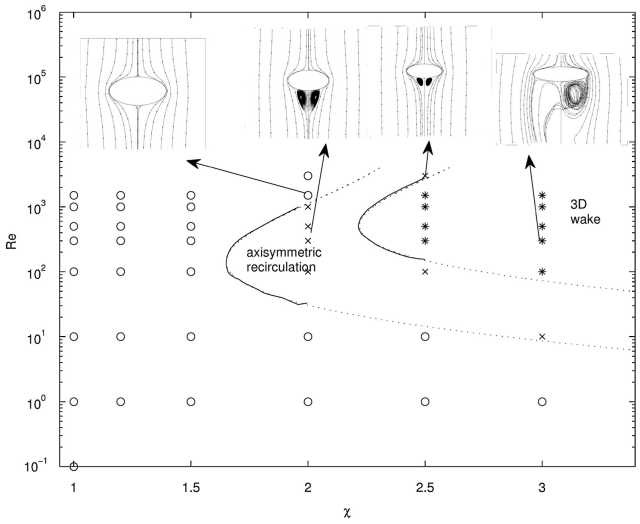

Figure 1.2: Re-χ-diagram, reproduced from [5].

In the following sections, the governing equations, the physical properties of the system, the numerical setup and the evaluation procedure are explained before the results are presented and interpreted.

2 Governing physical phenomena

2.1 Problem description and assumptions

The fluid's influence on the flow characteristics must be modelled mathematically. The most common law for fluids is "Newton's law of viscosity":

$$\underline{\underline{\tau}} = \frac{\eta}{\rho}(\nabla \underline{u} + \nabla \underline{u}^T) \tag{2.1}$$

It states that the shear stress $\underline{\underline{\tau}}$ in a fluid is proportional to the shear rate. The proportionality factor $\nu = \eta/\rho$ represents the fluid's kinematic viscosity. Fortunately, many common fluids, such as water, obey this law. In the following, the fluid is assumed to be a Newtonian fluid. All processes are assumed to be isothermal, i.e. they happen at constant temperature. In addition, the fluid is stated to be incompressible, i.e.

$$\frac{\partial \rho}{\partial t} = 0. \tag{2.2}$$

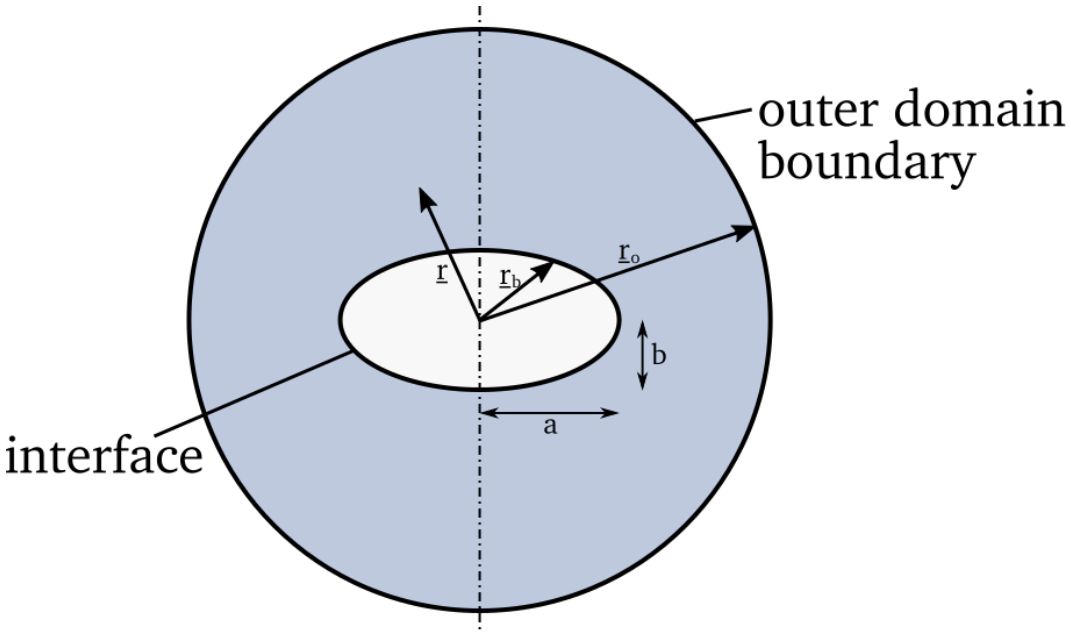

Figure 2.1: Sketch of the domain.

Figure 2.1 shows a sketch of the domain that is used. Here, a is the spheroid's semi-major axis, b the semi-minor axis and the ratio a/b equals the aspect ratio χ of the spheroid. The equivalent radius r_{eq} of the bubble is always 1 mm. The shape of the bubbles is created in such a way that the volume of the spheroid is always equal to the volume of a sphere with radius r_{eq}, that is

$$V_{eq} = V_{spheroid}, \tag{2.3}$$

$$\frac{4}{3}\pi r_{eq}^3 = \frac{4}{3}\pi a^2 \cdot b, \tag{2.4}$$

$$r_{eq}^3 = a^2 \cdot b = 1\,\mathrm{cm}^3. \tag{2.5}$$

The resulting radii a and b of the spheroids are calculated from (2.5). The concentration inside the bubble is assumed to be constant at $1\,\mathrm{mol\,m^{-3}}$ and fully mixed. The bubble is represented by a fixed surface without mesh inside. Around the bubble, a sphere with radius $r_o = 20 \cdot r_{eq}$ is used as the outer domain. This size is chosen to avoid wall effects influencing the flow field close to the bubble .

2.2 Governing equations

The transport of a diluted chemical species c in the absence of chemical reactions is governed by the following convection-diffusion equation:

$$\frac{\partial c}{\partial t} + \nabla \cdot (\underline{u}c) - \nabla \cdot (D\nabla c) = 0. \tag{2.6}$$

Here, c is the concentration of the species, $\underline{u}$ is the velocity vector of the liquid bulk and D is the molecular diffusivity of the species. The diffusive fluxes are approximated using Fick's law.

In (2.6), the velocity field $\underline{u}$ is provided by solving the Navier-Stokes Equations for Newtonian fluids:

$$\nabla \cdot \underline{u} = 0 \tag{2.7}$$

$$\frac{\partial \underline{u}}{\partial t} + \nabla \cdot (\underline{u}\underline{u}) = -\frac{1}{\rho}\nabla p + \nabla \cdot (\nu \nabla \underline{u}). \tag{2.8}$$

Here, ρ is the fluid's density and p is the pressure.

2.3 Boundary conditions

For the concentration c, and the fluid's velocity $\underline{u}$ and pressure p, boundary conditions have to be defined at the interface ($\underline{r} = \underline{r}_b$) and the outer domain boundary ($\underline{r} = \underline{r}_o$).

The flux of the transfer species is set to zero at the outer domain boundary:

$$\nabla c \cdot \underline{r}|_{\underline{r}=\underline{r}_o} = 0. \tag{2.9}$$

The concentration at the interface is defined as a fixed value:

$$c|_{\underline{r}=\underline{r}_b} = C_0. \tag{2.10}$$

For p the gradients at the interface and the outer domain boundary are also set to zero:

$$\nabla p|_{\underline{r}=\underline{r}_b, \underline{r}=\underline{r}_o} = \underline{0}. \tag{2.11}$$

For the velocity vector $\underline{u}$ at the interface, a slip condition is set, such that the liquid experiences no shear at the interface due to the difference in terms of viscosity [4]:

$$\underline{u} \cdot \underline{r}|_{\underline{r}=\underline{r}_b} = 0, \tag{2.12}$$

$$\underline{r} \times (\underline{\underline{\tau}} \cdot \underline{r})|_{\underline{r}=\underline{r}_b} = 0. \tag{2.13}$$

At the outer domain boundary, an *inlet-outlet* type boundary condition is applied to the velocity vector $\underline{u}$:

$$\underline{u}|_{\underline{r}=\underline{r}_o} = \underline{u}_{in} \quad for \quad \underline{u} \cdot \underline{r} \leq 0, \tag{2.14}$$

$$\nabla \underline{u}|_{\underline{r}=\underline{r}_o} = 0 \quad for \quad \underline{u} \cdot \underline{r} > 0. \tag{2.15}$$

3 Meshing strategies

3.1 Overview

Four different meshing strategies are compared with respect to accuracy, stability and run time. The meshing strategies are listed in Table 3.1.

Meshing strategy	Software
layered mesh with quadrilateral base	`blockMesh`
hexahedron-dominated mesh	`snappyHexMesh`
layered mesh with polygonal base	`Netgen` and `polyDualMesh`
polyhedra mesh	`Netgen` and `polyDualMesh`

Table 3.1: Overview of the meshing strategies.

The meshing strategies differ mainly in the shape of the cells that constitute the mesh. Each cell shape has certain characteristics that in turn can lead to advantages and disadvantages regarding the criteria of comparison. The bubble shape is created as an *STL* (Standard Tesselation Language) file using `salome`®[1]. The meshing processes are executed using `salome`® and the open source software `OpenFOAM`®[2] (Open Field Operation And Manipulation)

3.2 Layered mesh with quadrilateral base

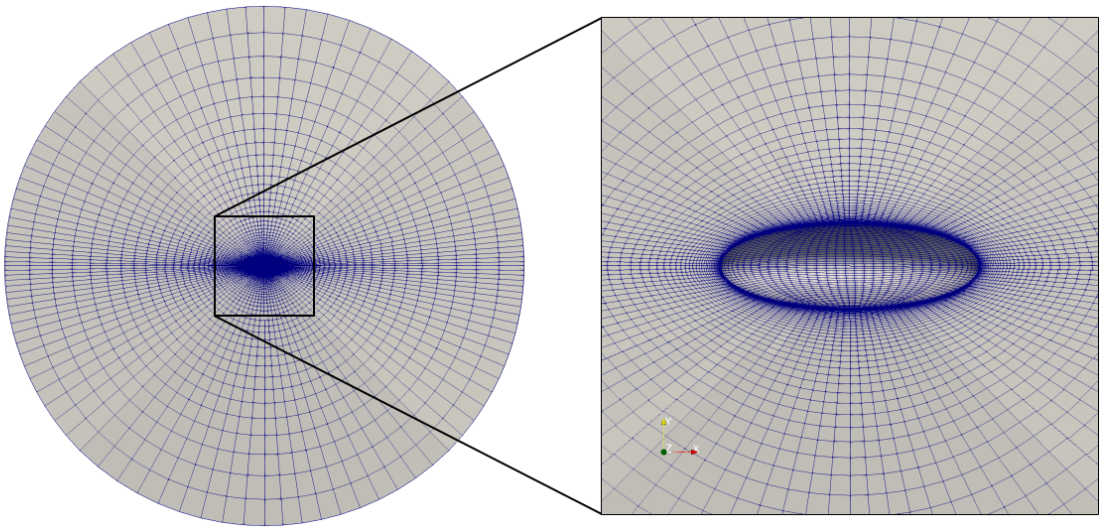

Figure 3.1: Layered mesh with *quadrilateral* base.

Layered meshes are created by extruding the surface mesh to the outer sphere. The `blockMesh` utility from `OpenFOAM`® creates cells with a quadrilateral base (Figure 3.1). The possibility of grading the layer thickness allows

[1] Link: `http://www.salome-platform.org/`
[2] Link: `https://www.openfoam.com/`

for the creation of smaller cells around the interface in order to resolve the steep gradients of velocity and species concentration, while the cells further away from the bubble are larger to reduce the total number of cells.
This method does not allow for the definition of a refinement region for the bubble wake which means that the mesh is either not fine enough in the wake or unnecessarily fine in other regions.

3.3 Hexahedron-dominated mesh

Hexahedron-dominated meshes (Figure 3.2) are created using the `snappyHexMesh` utility from `OpenFOAM®`. The way `snappyHexMesh` works is that it makes specific changes to a previously defined hexahedra background mesh. The latter has to cover all outer boundaries of the domain. A single block with a side length of 0.044 m created with `blockMesh` is utilized.
All parameters for the actual meshing are stored in a file called *snappyHexMeshDict*, which contains the necessary geometry and three subdictionaries. The geometry of the bubble is imported from the STL file. By means of predefined functions, a certain distance from the interface and a cylinder around the wake are defined as refinement regions. In the *castellatedMeshControls* subdictionary the refinement process is determined by defining levels of refinement. Each level of refinement splits a hexahedron into eight identical smaller hexahedra. After the castellation, the cells inside the bubble and around the outer sphere are removed.
The next step is the snapping process controlled by the *snapControls* subdictionary. The castellated mesh at the boundaries of the refined region is adapted to the surface defined in the STL files. The quality of the mesh after the snapping process has to be monitored, especially at the bubble interface.
The boundary layers are defined by four entries in the *addLayersControls* subdictionary: the number of layers, the expansion ratio of layer thicknesses, the overall layer thickness and the minimum thickness of a single layer.
While the mesh creation in `snappyHexMesh` can already be executed in parallel the meshes created with the other strategies can only be decomposed after the mesh creation.

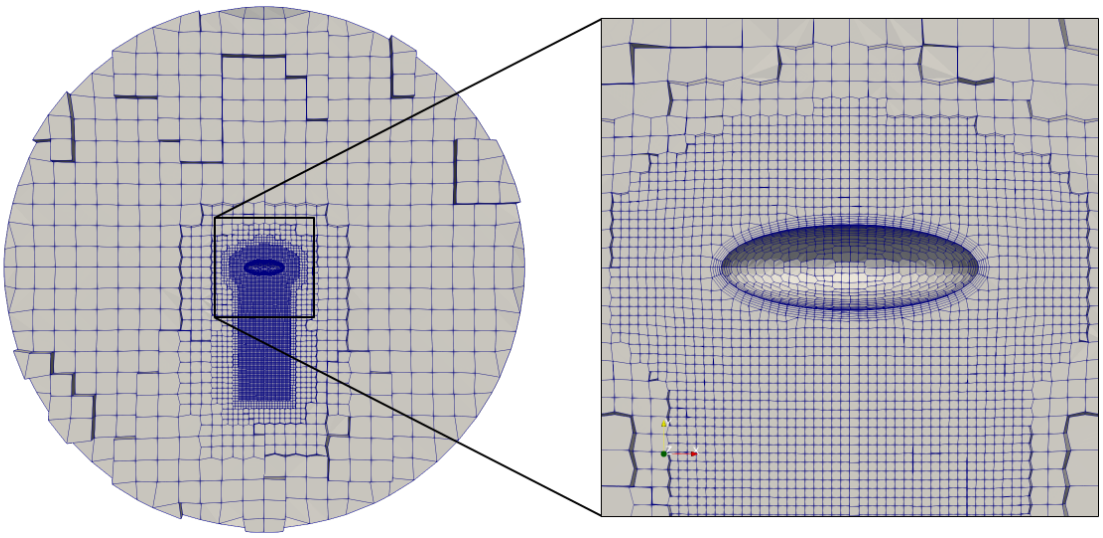

Figure 3.2: Hexahedron-dominated mesh.

3.4 Layered mesh with polygonal base

The layered meshes with polygonal base (Figure 3.3) are created using `salome®` and `OpenFOAM®`. In `salome®`, the bubble surface and the outer sphere are triangulated using the `NETGEN-1D-2D` algorithm. The triangles are extruded from the interface to the outer sphere, creating a prismatic mesh with triangular base. Finally, the tetrahedra are

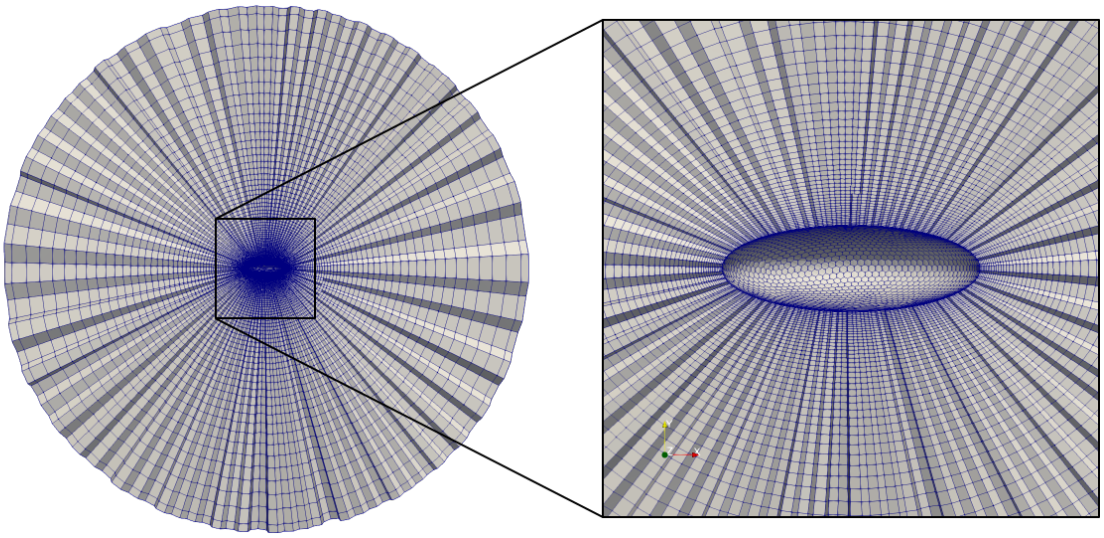

Figure 3.3: Layered mesh with polygonal base.

transformed into polyhedra using the `polyDualMesh` utility from `OpenFOAM®`.
Similarly to the layered mesh with quadrilateral base, the mesh grading is the only way of concentrating cells around the interface and no wake refinement can be defined.

3.5 Polyhedra mesh

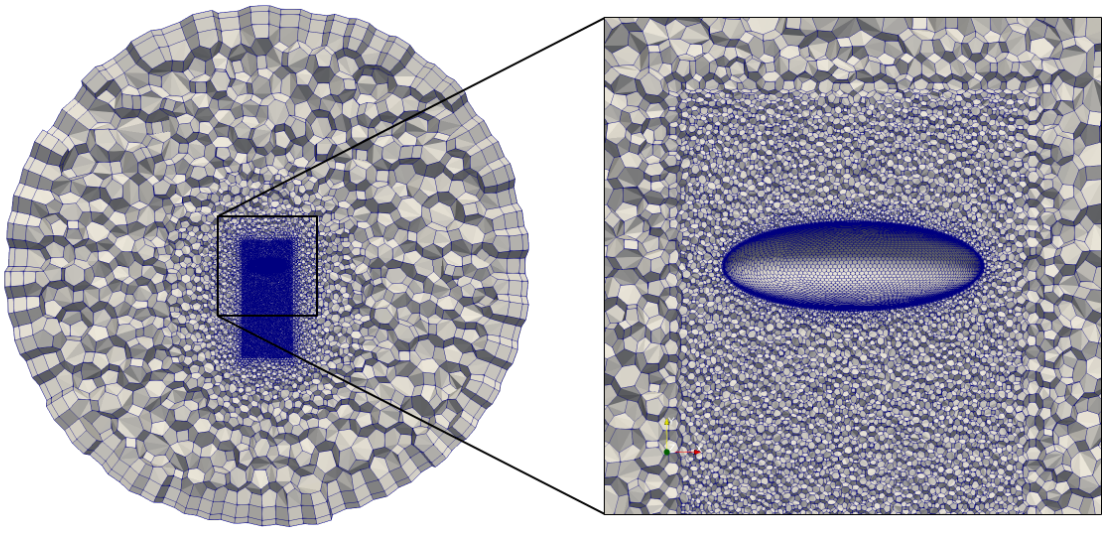

Figure 3.4: Polyhedra mesh.

For the polyhedra mesh (Figure 3.4) the surfaces are triangulated similarly to the layered meshes with polygonal base. However, in this case, the volume mesh is created using the `NETGEN-3D` algorithm. First, prismatic boundary layer cells with triangular base are extruded from the interface. The remaining volume is triangulated, too. In the refinement regions, the tetrahedra are split to get smaller cells. The last step is again the transformation of the tetrahedra into polyhedra via the `polyDualMesh` utility from `OpenFOAM®`.
The desired mesh resolution is obtained by changing the approximate side lengths of the cells on the surfaces and in the volume mesh. Additionally, boundary layers and a refinement region for the wake can be defined like in

`snappyHexMesh`. The mesh in Figure 3.4 has five layers around the bubble, but their total thickness is $0.02 \cdot r_b$, which is why they are not recognizable in the picture.

3.6 Meshing characteristics

In Table 3.2, some aspects and characteristics of the meshing process are summarized and compared between the strategies.

	Layered mesh with quadrilateral base	**Hexahedron-dominated**	**Layered mesh with polygonal base**	**Polyhedron-dominated**
Layer addition	• Layers are part of the volume mesh • Outcome exactly as defined in the dictionary	• After volume meshing • Outcome is influenced by geometry and mesh quality criteria	• Layers are part of the volume mesh • First layer is split in half by `polyDualMesh`	• Before volume meshing • First layer is split in half by `polyDualMesh`
Volume Mesh	• Wake refinement only by refining whole mesh • Outcome exactly as defined in the dictionary	• Refinement regions defined as geometries • Outcome is influenced by geometry and mesh quality criteria • Creation of concave cells in transition regions between refinement levels • Fine tuning of mesh size either by changing the background mesh or increasing the refinement level	• Wake refinement only by refining whole mesh	• Refinement regions defined as geometries • Creation of concave cells by `polyDualMesh` (randomly distributed)
Computational cost	• Lowest, fastest creation process • No parallelization possible and necessary	• Higher than for layered meshes • Parallelization is simple	• Higher than for layered mesh with quadrilateral base but lower than for hex-dominated and polyhedra meshes • No parallelization possible	• Highest, slowest creation process • No parallelization possible
Accuracy	• Double precision (up to 16 decimal places) • Accurate approximation of input geometry	• Double precision • Sometimes poor approximation of input geometry due to mesh quality criteria	• Accuracy limited to single precision (up to 8 decimal places) • Accurate approximation of input geometry	• Accuracy limited to single precision • Accurate approximation of input geometry

Table 3.2: Characetristics of the meshing strategies.

4 Setup

4.1 Numerical setup

The Navier-Stokes equation (2.8) has to be solved in order to get the flux field required to calculate species transport. Boundary conditions for $\underline{u}$, p and c as defined in OpenFOAM® are summarized in Table 4.1. The schemes that are used to dicretize the momentum equation and convection-diffusion equation (2.6) are summarized in Table 4.2 and Table 4.3, respectively. The tolerances of the iterative solvers are listed in Table 4.4.

Boundary	$\underline{u}$	p	c
Interface	inletOutlet	zeroGradient	fixedValue
Outer sphere	slip	zeroGradient	zeroGradient

Table 4.1: OpenFOAM® boundary conditions in the simulations.

Scheme	**Type**
ddtSchemes	Euler
gradSchemes	Gauss linear
divSchemes	Gauss linearUpwind grad(U)
laplacianSchemes	Gauss linear corrected
interpolationSchemes	linear
snGradSchemes	corrected

Table 4.2: Discretization schemes for the momentum equation.

Scheme	**Type**
ddtSchemes	Euler
gradSchemes	Gauss linear
divSchemes	Gauss limitedLinear01 0.5
laplacianSchemes	Gauss linear corrected
interpolationSchemes	linear
snGradSchemes	corrected

Table 4.3: Discretization schemes for the species transport equation.

Parameter	Solver	Tolerance
c	PBiCGStab	$1 \cdot 10^{-9}$
p	GAMG	$1 \cdot 10^{-6}$
$\underline{u}$	smoothSolver	$1 \cdot 10^{-7}$

Table 4.4: Iterative solvers and respective tolerances.

The simulations are executed using the reactingPisoFoam (piso=pressure-implicit split-operator) solver from OpenFOAM® that is used in transient problems to couple momentum and mass conservation equation. The initial solution is provided by the potentialFoam utility. All four meshing strategies can be run in parallel which means that the domains are divided into smaller subdomains that are calculated on different cores. The decomposition is done using the scotch algorithm from OpenFOAM®. The *coarse* meshes are decomposed into four subdomains, the *medium* meshes into eight and the *fine* meshes into sixteen subdomains. Mesh properties are obtained with the checkMesh utility from OpenFOAM®, which has an integrated mesh quality evaluation.

4.2 Design of Experiment

First, for each of the four meshing strategies, setups with $\chi = 3$, $Re = 500$ and $Sc = 100$ are simulated. The discretization of (2.6) entails the presence of discretization errors that have the greatest impact in areas with steep concentration gradients, i.e. the vicinity and the wake of the bubble. To make statements about mesh sensitivity, the results of a setup with a reasonable solution are compared to the results of finer meshes. If the results change less than a previously defined limit of percentage it is assumed that the results are independent from the mesh. Therefore, for each mesh type three setups with different amounts of cells are tested. The cases *coarse*, *medium* and *fine* of each mesh type are set up in such a way that they have a comparable number of cells.
The first attempt was, to define the different mesh sizes by increasing the refinement level in the refinement regions of the hexahedron-dominated mesh. This means, for example, that the *medium* mesh is created by dividing each cell in the refinement region of the *coarse* mesh into eight cells. However, this results in the *fine* hexahedron-dominated mesh having about $34 \cdot 10^6$ cells. Even though a solution with such a mesh could be calculated using parallel processing, the computational effort exceeds the scope of the present work.
Instead, three mesh sizes, 200 000, 400 000 and 800 000 cells, are defined and the meshes are adjusted to the prescribed number of cells. The cell number of the hexahedron-dominated mesh is now manipulated by decreasing the cell size of the background mesh or increasing the refinement level and simultaneously increasing the cell size of the background mesh. The other meshes are manipulated in different ways:

- For the layered meshes, the mesh size is increased by raising the number of cells in radial and tangential direction while the ratio n_{rad}/n_{tan} should stay approximately constant. This is important because increasing only the cell number in radial direction eventually leads to thin cells with high aspect ratios, which can cause numerical problems.
- For the polyhedra mesh, the mesh size is increased by decreasing the edge lengths of the tetrahedra on the surfaces and in the volume.

The comparison of the meshes with regard to stability, accuracy and run time requires the definition of comparison criteria that allow statements about the advantages and disadvantages of the meshing strategies. As an indication of the stability of the computations the Courant number Co is used. It is defined as

$$Co = \frac{u\Delta t}{\Delta x}, \tag{4.1}$$

where Δx is the edge length of a cell. The maximum value for the Courant number occurrs at the cells with the smallest edge length, which are the cells in the first layer around the bubble.
The maximum Courant number is calculated and displayed for every iteration of the `reactingPisoFOAM` solver. The goal is to ensure $Co < 1$ everywhere and at all times. The time increment is set in such way that the maximum Courant number of the first iteration lies around 0.5 or at least between 0.2 and 0.8.
The quality of the meshes is evaluated. The cells' non-orthogonality and skewness are two mesh characteristics with a significant influence on both, the accuracy and the stability of the results. Specifically, non-orthogonalities above 50 can lead to stability issues. That is why these key figures are subject to a closer investigation.
The main criterion to evaluate the accuracy of the computations is the global Sherwood Sh number, which is calculated as the area-weighted integral of the local Sherwood numbers Sh_{loc},

$$Sh_{eff}(\chi) = \frac{1}{\partial V} \int_{\partial V} Sh_{loc} dA. \tag{4.2}$$

Next, the integral scale of segregation, see [1],

$$\varphi(V) = \frac{1}{|V|} \int \|\nabla f\| dV \tag{4.3}$$

is evaluated as a measure of the captured wake structures. In (4.3), $|V|$ is the volume of the averaging range, in this case a cylinder of 1.8 mm radius around the bubble wake, $f = c/c_{max}$ is the normalized concentration and $\|\nabla f\|$ the Euclidean length of its gradient. φ can be interpreted as the volume-referred total variation of the normalized concentration field and is hence appropriate to measure if all relevant length scales are covered [2]. With a decreasing cell size, smaller structures are resolved and φ rises as long as the actual solution still holds smaller structures. After that, the concentration field and the streamline plot of each setup are analyzed to evaluate the flow patterns that form. Because three-dimensional flow fields are expected, the concentration fields are visualized in two orthogonal cross sections.
Time performance is evaluated by investigating the run- and the CPU-time of the `reactingPisoFOAM` solver. The *medium* meshes are used and each setup is tested using one, two, four and eight processors.
The run-time equals the clocktime that is displayed at the end of the last iteration. The CPU-time is calculated by multiplying the run-time with the number of processors used.
The run-time indicates how much time a certain mesh type needs for a given number of iterations compared to the other mesh types. The CPU-time shows how well the run-time reduction scales with the number of processors.
Subsequently, the mesh that shows the best results is used for studies with other Reynolds numbers and Schmidt numbers.

5 Results

5.1 Stability and accuracy

All setups ran stable until the defined end time. At the beginning of each computation the maximum Courant number drops in all setups. This is because the first solution is calculated based on potential flow theory. The highest and average maximum Courant numbers are summarized in Table 5.1. The Courant numbers of the hexahedron-dominated meshes display the most significant drop.

	Layered mesh with quadrilateral base	**Hexahedron-dominated**	**Layered mesh with polygonal base**	**Polyhedron-dominated**
coarse	0.4132 / 0.3579	0.5182 / 0.1930	0.7770 / 0.7226	0.6309 / 0.6097
medium	0.5264 / 0.4463	0.6765 / 0.3227	0.5255 / 0.5015	0.4767 / 0.4431
fine	0.6578 / 0.5596	0.4301 / 0.2261	0.5307 / 0.5080	0.4937 / 0.4675

Table 5.1: Highest and average maximum Courant numbers.

5.1.1 Mesh quality

Important statistics and properties of the meshes for $\chi = 3$ are summarized in Table 5.2. The target of comparable mesh sizes leads to a wide range of boundary layer thicknesses between the meshing strategies. The aim is always to adjust the boundary layer cells to the thicknesses estimated in chapter 1 but simultaneously to keep the non-orthogonalities below the value of 50° and to pass the quality evaluation by the `checkMesh` utility. The boundary layers of the hexahedron-dominated meshes are as small as possible given the size of the refinement area and the equal refinement level of surface and volume mesh. Reducing the final layer thickness or increasing the layer aspect ratio or the amount of layers lead to the problem that `snappyHexMesh` does not create the layers properly because of the internal mesh quality criteria. Ultimately, the hexahedron-dominated meshes have the fewest cells in their boundary layer. For the layered meshes, increasing the radial grading would lead to failed mesh checks. In contrast, the layer addition in the polyhedra meshes does not affect the quality of the mesh and the sizes can be adjusted abitrarily. Only with this strategy the postulated goal of five cells in the first $8\,\mu$m around the bubble is (approximately) achieved. The layered meshes with polygonal base have non-orthogonalities above the declared aim of 50°. This does not affect the stability of the computations in this case but can influence the accuracy of the results. All meshes except for the polyhedra ones pass the quality checks from `checkMesh`. In Figure 5.1 to Figure 5.3, the non-orthogonalities of the twelve tested meshes are shown.

	Layered mesh with quadrilateral base	Hexahedron-dominated	Layered mesh with polygonal base	Polyhedron-dominated
Mesh size	coarse: 205770 medium: 407808 fine: 810000	coarse: 205982 medium: 414856 fine: 812131	coarse: 205829 medium: 407440 fine: 807120	coarse: 203872 medium: 404879 fine: 799100
Faces per cell (average)	6	6.12	8	12.32
Maximum skewness	coarse: 0.7071 medium: 0.6507 fine: 0.6789	coarse: 0.7446 medium: 0.70307 fine: 0.7310	coarse: 0.5409 medium: 0.4997 fine: 0.3866	coarse: 1.122 medium: 1.129 fine: 1.214
Maximum/average non-orthogonality	coarse: 48.11/19.82 medium: 48.72/19.80 fine: 49.43/20.76	coarse: 39.98/3.92 medium: 42.28/3.50 fine: 41.43/2.839	coarse: 54.77/16.30 medium: 55.09/16.58 fine: 55.57/16.44	coarse: 44.37/10.12 medium: 44.11/9.870 fine: 46.04/9.752
Thickness of the first/first five cell(s) in radial direction	coarse: 5.8 μm/27.6 μm medium: 4.2 μm/20.6 μm fine: 3.3 μm/15.8 μm	coarse: 23.7 μm/122.2 μm medium: 17.7 μm/94.4 μm fine: 8.5 μm/43.5 μm	coarse: 11.2 μm/80.3 μm medium: 8.0 μm/58.4 μm fine: 4.2 μm/32.3 μm	coarse: 2.5 μm/26.4 μm medium: 1.3 μm/10.8 μm fine: 1.0 μm/10.5 μm
Time increment/maximum Co at the beginning	coarse: $1.0 \cdot 10^{-5}$/0.4132 medium: $1.0 \cdot 10^{-5}$/0.5264 fine: $1.0 \cdot 10^{-5}$/0.6578	coarse: $5.0 \cdot 10^{-5}$/0.5182 medium: $5.0 \cdot 10^{-5}$/0.6765 fine: $2.5 \cdot 10^{-5}$/0.4301	coarse: $5.0 \cdot 10^{-5}$/0.7770 medium: $2.5 \cdot 10^{-5}$/0.5255 fine: $2.0 \cdot 10^{-5}$/0.5307	coarse: $2.0 \cdot 10^{-5}$/0.6285 medium: $5.0 \cdot 10^{-6}$/0.4739 fine: $5.0 \cdot 10^{-6}$/0.4929

Table 5.2: Properties and statistics of the used meshes.

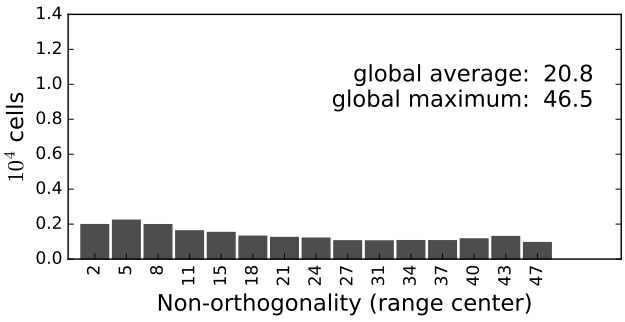

(a) Layered, quadrilateral base

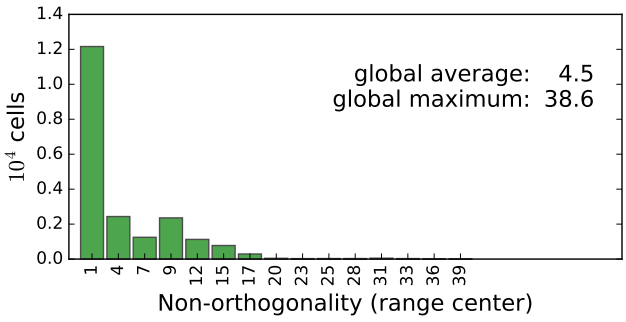

(b) Hexahedron-dominated

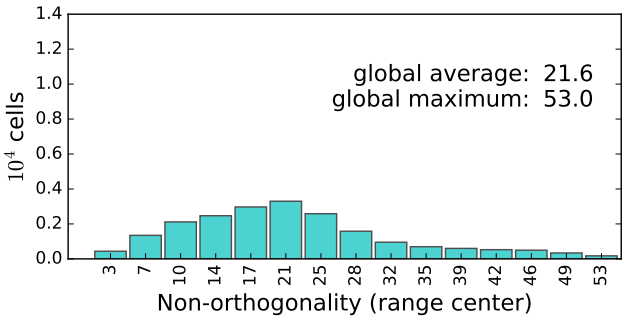

(c) Layered, polygonal base

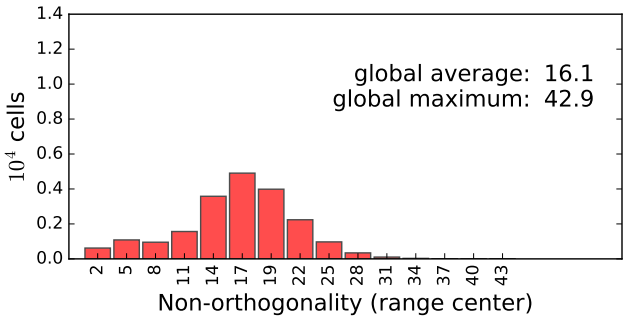

(d) Polyhedra

Figure 5.1: Non-orthogonality of the *coarse* meshes.

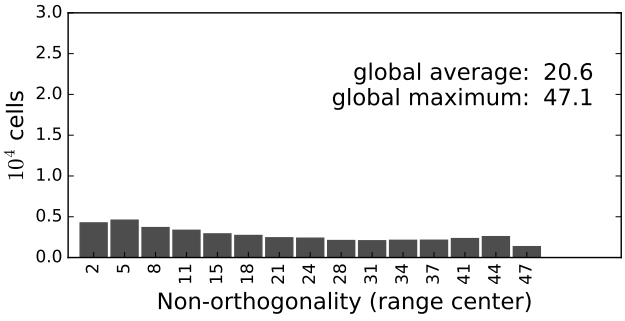

(a) Layered, quadrilateral base

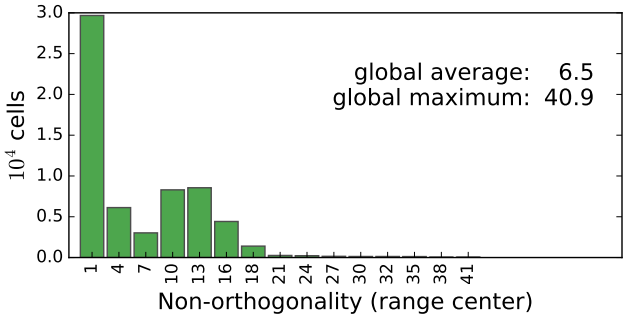

(b) Hexahedron-dominated

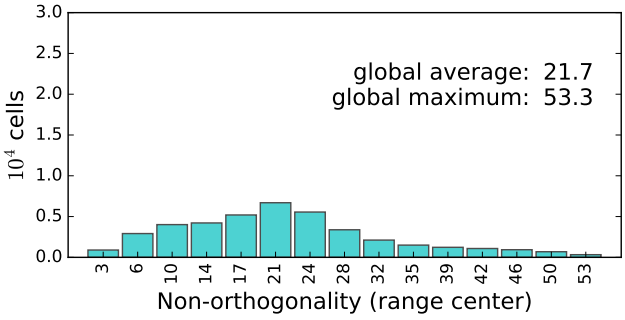

(c) Layered, polygonal base

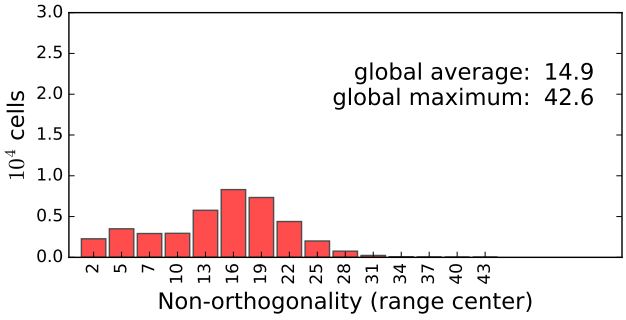

(d) Polyhedra

Figure 5.2: Non-orthogonality of the *medium* meshes.

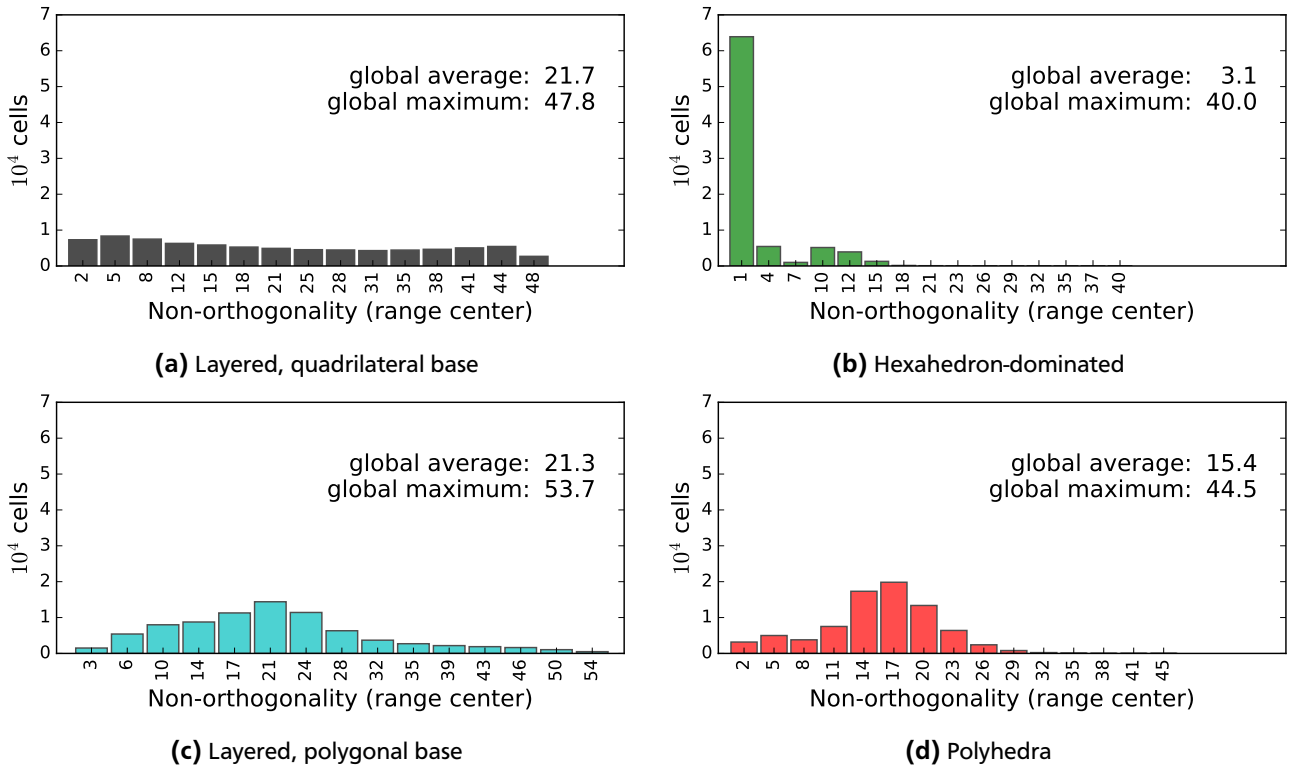

(a) Layered, quadrilateral base

(b) Hexahedron-dominated

(c) Layered, polygonal base

(d) Polyhedra

Figure 5.3: Non-orthogonality of the *fine* meshes.

Independent from the mesh size, the hexahedron-dominated meshes have the lowest maximum and average non-orthogonalities. Most of the cells are concentrated around 1° which means that the majority of cells have very low non-orthogonalities. The average non-orthogonality value of *fine* hexahedron-dominated mesh is 31.1 % below the value of the *coarse* and 52.3 % below the value of the *medium* mesh. All three layered meshes with polygonal base have the highest occurring non-orthogonalities, which lie around 53°. The average values of those meshes lie around 21° which is similar to the layered meshes with quadrilateral base, although in the latter the maximum values lie around 47°. The non-orthogonalities of the layered meshes with polygonal base and the polyhedra meshes have their peak in the middle of the distribution, while the layered meshes with qudrilateral base show peaks at low and high numbers. The tendencies of the differently sized meshes of one meshing strategy qualitatively show the same behaviour. Differences are mainly of quantitative nature. The average values are compared in Table 5.3 with regard to the lowest occurring value, as quantification of the differences between non-orthogonalities. The deviations from the lowest value are the highest for the *fine* meshes.

	Layered mesh with quadrilateral base	**Hexahedron-dominated**	**Layered mesh with polygonal base**	**Polyhedra**
coarse	+362 %	0 %	+380 %	+258 %
medium	+217 %	0 %	+234 %	+129 %
fine	+600 %	0 %	+587 %	+397 %

Table 5.3: Deviations of average non-orthogonalities from lowest value.

A similar evaluation of the cells' *skewnesses* is carried out; see Figure 5.4 to Figure 5.6.

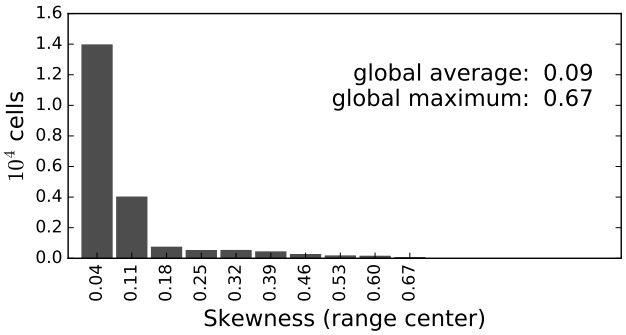

(a) Layered, quadrilateral base

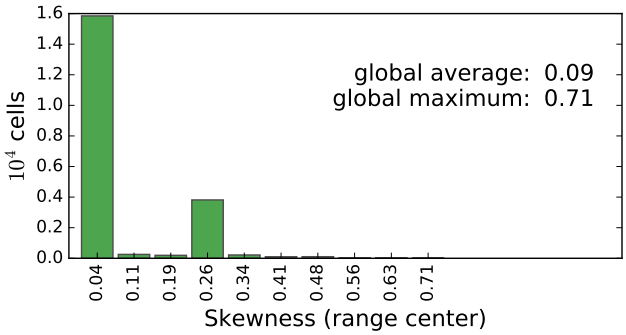

(b) Hexahedron-dominated

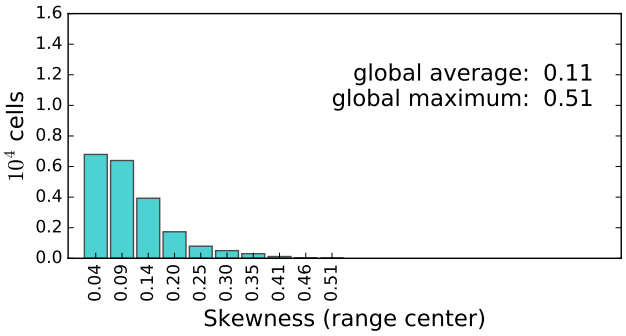

(c) Layered, polygonal base

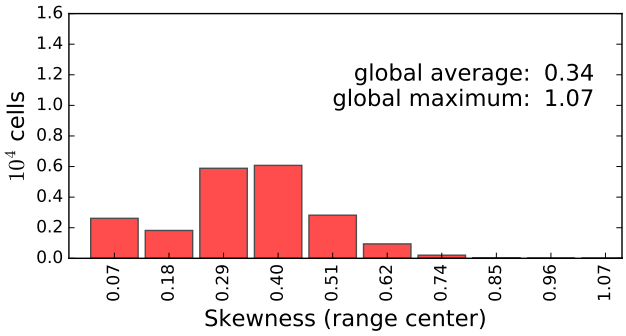

(d) Polyhedra

Figure 5.4: Skewness of the *coarse* meshes.

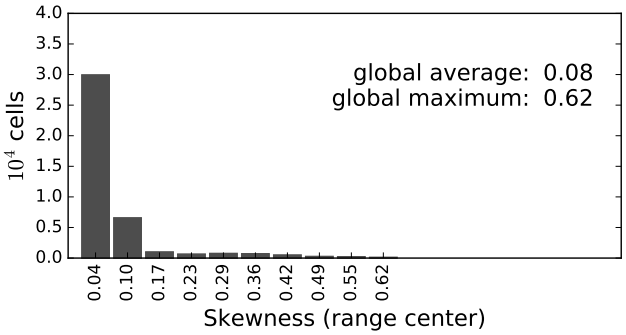

(a) Layered, quadrilateral base

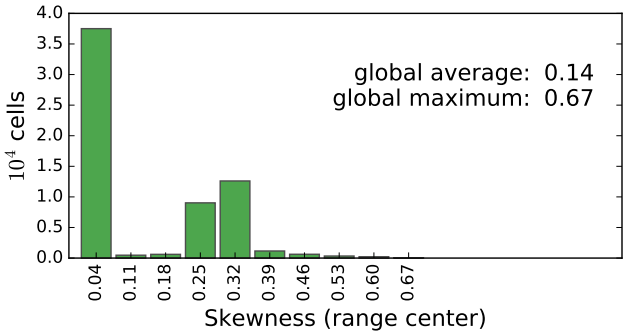

(b) Hexahedron-dominated

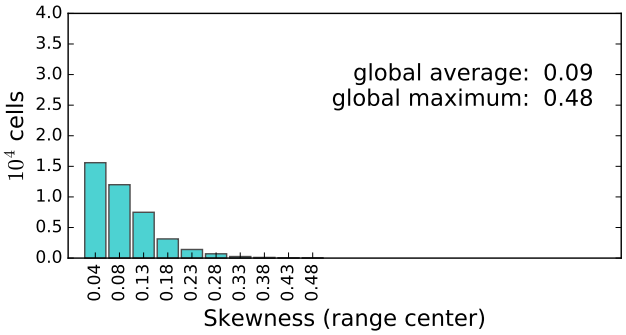

(c) Layered, polygonal base

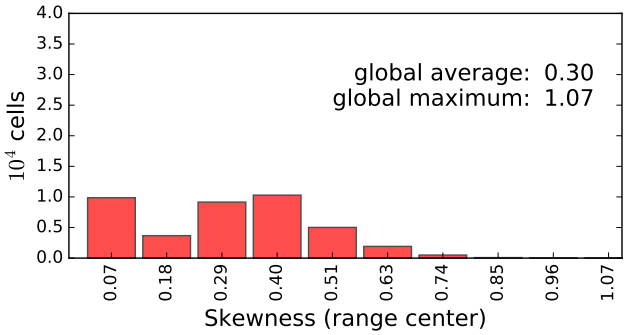

(d) Polyhedra

Figure 5.5: Skewness of the *medium* meshes.

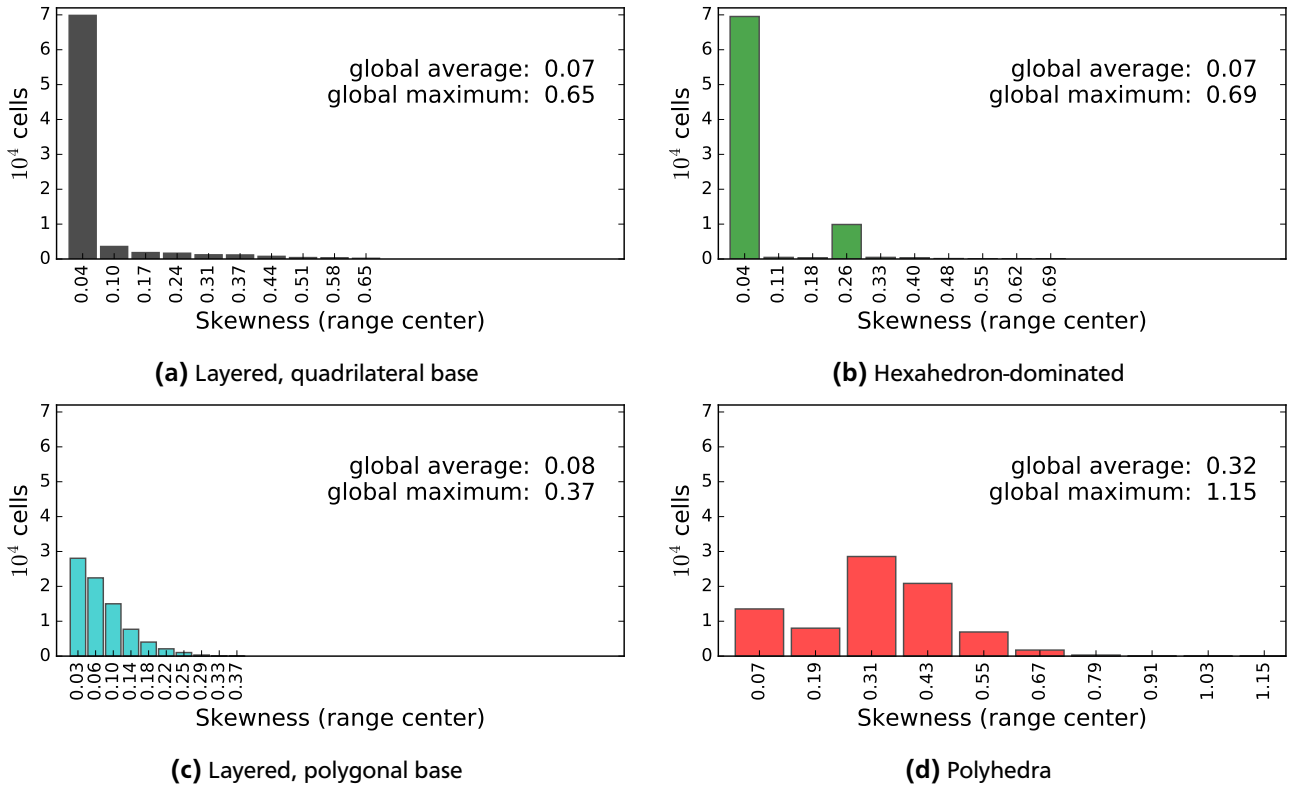

(a) Layered, quadrilateral base

(b) Hexahedron-dominated

(c) Layered, polygonal base

(d) Polyhedra

Figure 5.6: Skewness of the *fine* meshes.

Both average and maximum skewness are highest in all three polyhedra meshes. The layered meshes with polygonal base have the lowest maximum skewness. Again, the values for meshes of one meshing strategy differ largely quantitatively. Equally to Table 5.3, the average skewnesses are compared in Table 5.4. The results emphasize the uncertainties, which the generation of the hexahedron-dominated meshes features.

	Layered mesh with quadrilateral base	**Hexahedron-dominated**	**Layered mesh with polygonal base**	**Polyhedra**
coarse	0 %	0 %	+22.2 %	+278 %
medium	0 %	+75.0 %	+12.5 %	+275 %
fine	0 %	0 %	+14.3 %	+357 %

Table 5.4: Deviations of average skewnesses from lowest value.

Concave cells in polyhedra mesh

Problems in the polyhedra meshes are not only posed by the high skewnesses but also the concavity of some cells. In the *coarse*, *medium* and *fine* setups 1680, 2873 and 4662 cells do not pass the mesh check which equals 0.82 %, 0.71 % and 0.58 % of the total cell number, respectively. Responsible for the concave cells is the `polyDualMesh` utility that creates the polyhedra from the tetrahedra mesh. The cells are distributed all over the domain, although a concentration in the refinement box is observed. However, no concentration around the bubble is visible. Thus the cell size might have an influence on the problem as it is the only characteristic that distinguishes the cells inside and outside the refinement box. The concave cells have no negative impact on the stability of the computations in

this case. The distribution of the ill-shaped cells in the *coarse* and in the *fine* mesh is shown in Figure 5.7.

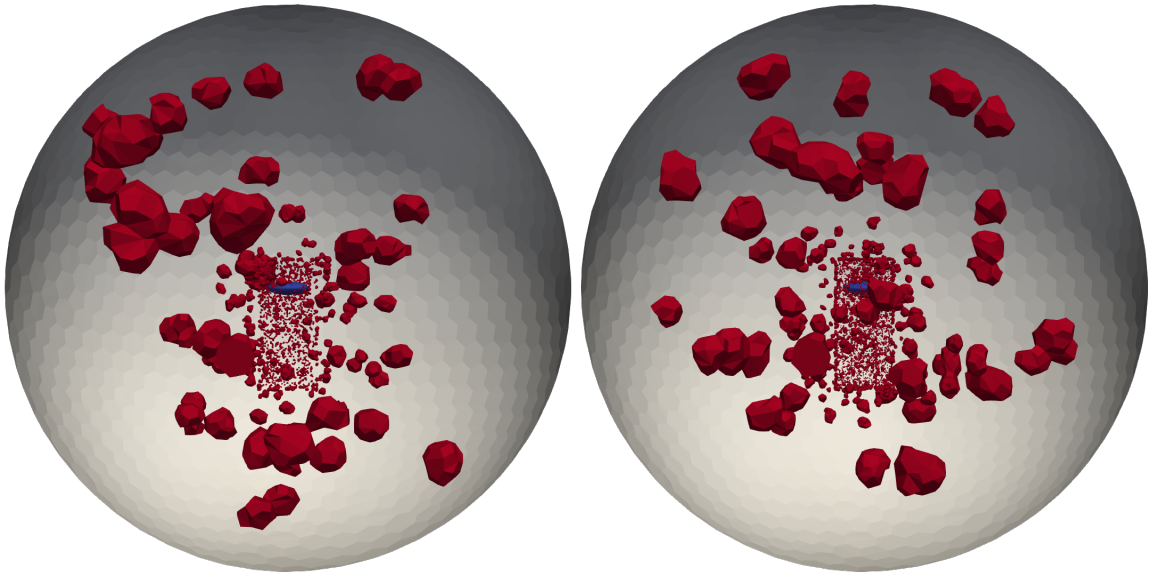

(a) *coarse* **(b)** *fine*

Figure 5.7: Concave cells of the polyhedra mesh.

5.1.2 Global Sherwood number

As mentioned in chapter 4, the global Sherwood number is considered to evaluate the accuracy of the simulation results. With respect to the fact that in setups with different Reynolds numbers the fluid has different velocities it is sensible to introduce a dimensionless time defined as $t^* = t \cdot U_b/d_b$. In Figure 5.8 the global Sherwood numbers are reported as functions of the dimensionless time t^*. The post-processing utility refers the global Sherwood numbers to the effective surface which is why they are converted to equivalent Sherwood numbers using the relation $Sh_{eq}(\chi) = Sh_{eff}(\chi) \cdot A_{eff}/A_{eq}$. $Sh_{eff}(\chi)$ is calculated from (4.2). In the following, the global Sherwood number Sh is always the equivalent Sherwood number Sh_{eq}. The reference is calculated using the expression $Sh_{eq}(\chi = 1) = 2 \cdot \sqrt{Pe}/\sqrt{\pi}$ from chapter 1 and the correction factor $Sh_{eq}(\chi)/Sh_{eq}(\chi = 1) = 0.524 + 0.88\chi - 0.49\chi^2 + 0.086\chi^3$ that is proposed in [4] to account for the effect of the aspect ratio. The results of the *layered* meshes and the *polyhedra* meshes are presented in an enlarged view, Figure 5.9, for a better understanding.

Most remarkable is the difference between the results of the hexahedron-dominated meshes and the other three meshing strategies. The global Sherwood numbers of the layered meshes and the polyhedra mesh are straighter and have less perturbations than those of the hexahedron-dominated meshes. Moreover, these results all lie between $Sh_{eq} = 280$ and $Sh_{eq} = 310$ while the global Sherwood numbers of the hexahedron-dominated meshes stay below $Sh_{eq} = 260$.

The layered meshes and polyhedra mesh reach a constant value at a certain time. For example, the *coarse* polyhedra mesh reaches the constant state around $t^* = 25$. In general, it applies that the finer the mesh, the later the constant state is reached. The only exceptions are the *coarse* and *medium* meshes, which reach the constant state at about the same time. The *medium* and *fine* polyhedra mesh reach the same value as the final constant. The same occurs for the *medium* and *fine* layered mesh with quadrilateral base. However, the solution from the *coarse* polyhedra mesh lies below *medium* and *fine* solution, whereas the solution from the *coarse* layered mesh with quadrilateral base lies above the finer solutions of this meshing strategy. With regard to the layered meshes with polygonal base

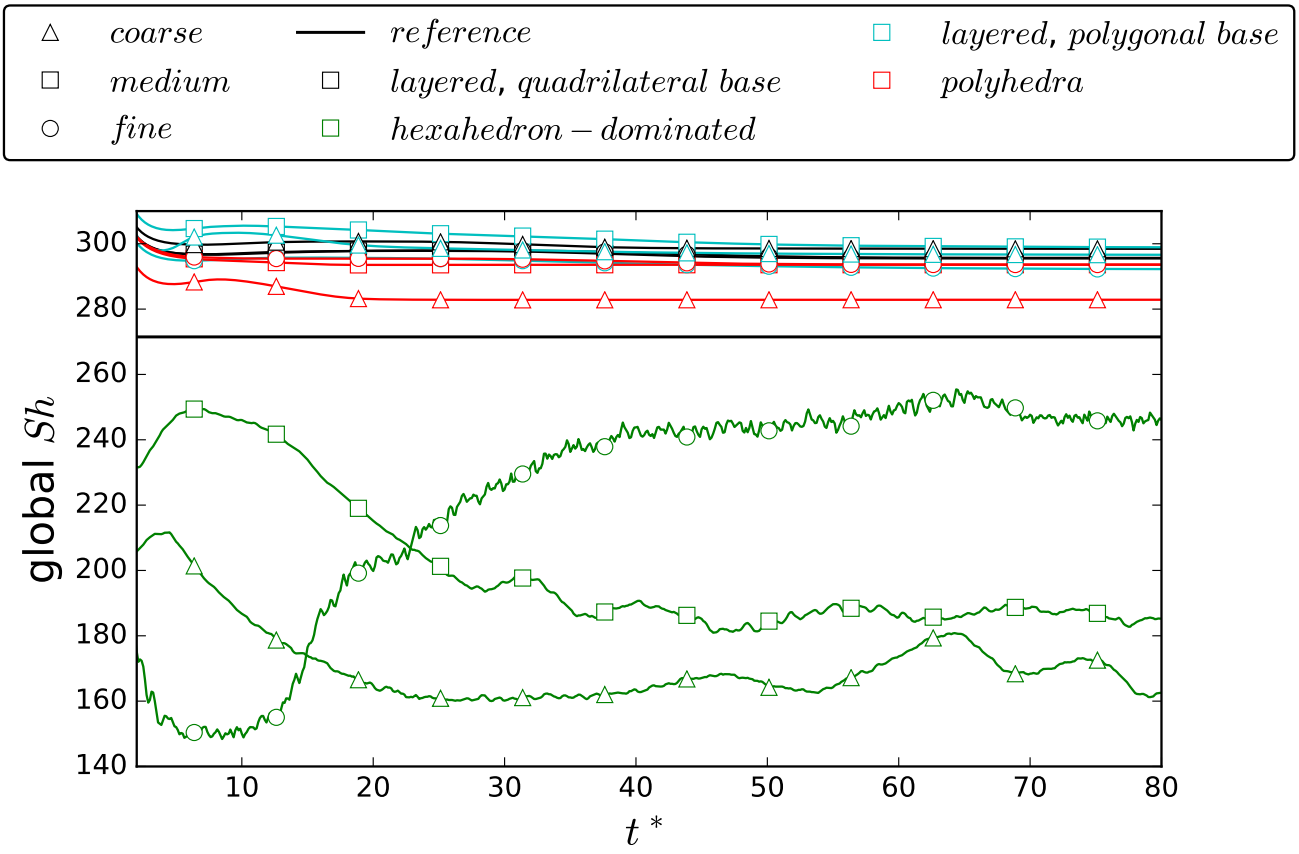

Figure 5.8: Global Sherwood numbers as functions of the dimensionless time.

the order of the mesh sizes top down is *medium*, *coarse* and *fine*.

All three *coarse* meshes in Figure 5.9 have a local minimum and maximum before converging. This behaviour is less or not at all detectable for the *medium* and *fine* meshes.

The results of the hexahedron-dominated meshes are not as steady but show small fluctuations that are most distinctive for the *fine* mesh. The trend of the *coarse* mesh first falls to a value around $Sh_{eq} = 160$ but around $t^* = 40$ uneven cyclical fluctuations start. The graph of the *medium* mesh lies above the *coarse* result but qualitatively shows the same trend. The graph of the *fine* mesh is the lowest at the beginning but rises to the highest and converges around a value of approximately $Sh_{eq} = 240$. The graph has its global maximum at $t^* \approx 65$.

The reason for the differences could be a different resolution of the hydrodynamics. The number of iterations the `reactingPisoFOAM` solver needs for pressure, velocity and species concentration can be an indicator for that. For example, at $t^* = 40$ of the *coarse* layered mesh with quadrilateral base the solver calculates no solutions for the velocity field, one iteration for one of six pressure field solutions and one iteration for one of three concentration field solutions (no iterations for the remaining solutions). The results enter a stationary state. The layered meshes with polygonal base show a similar behaviour. In the polyhedra meshes only the solutions for velocity and concentration field reach a stationary state.

The reference solution lies below the results of the layered and polyhedra meshes and above the results of the hexahedron meshes. In [4] it is reported that for higher aspect ratios the agreement between the reference and the actual solution declines.

Obviously, the results for the global Sherwood number are still dependent on the mesh resolution. The differences between the hexahedron-dominated and the other meshes highlight the significance of the surface mesh and the boundary layer cells for the solution. The layered and the polyhedra meshes have a uniform surface mesh in common in terms of cell shape and size of the boundary layer cells. Moreover, the boundary layer cells are smaller

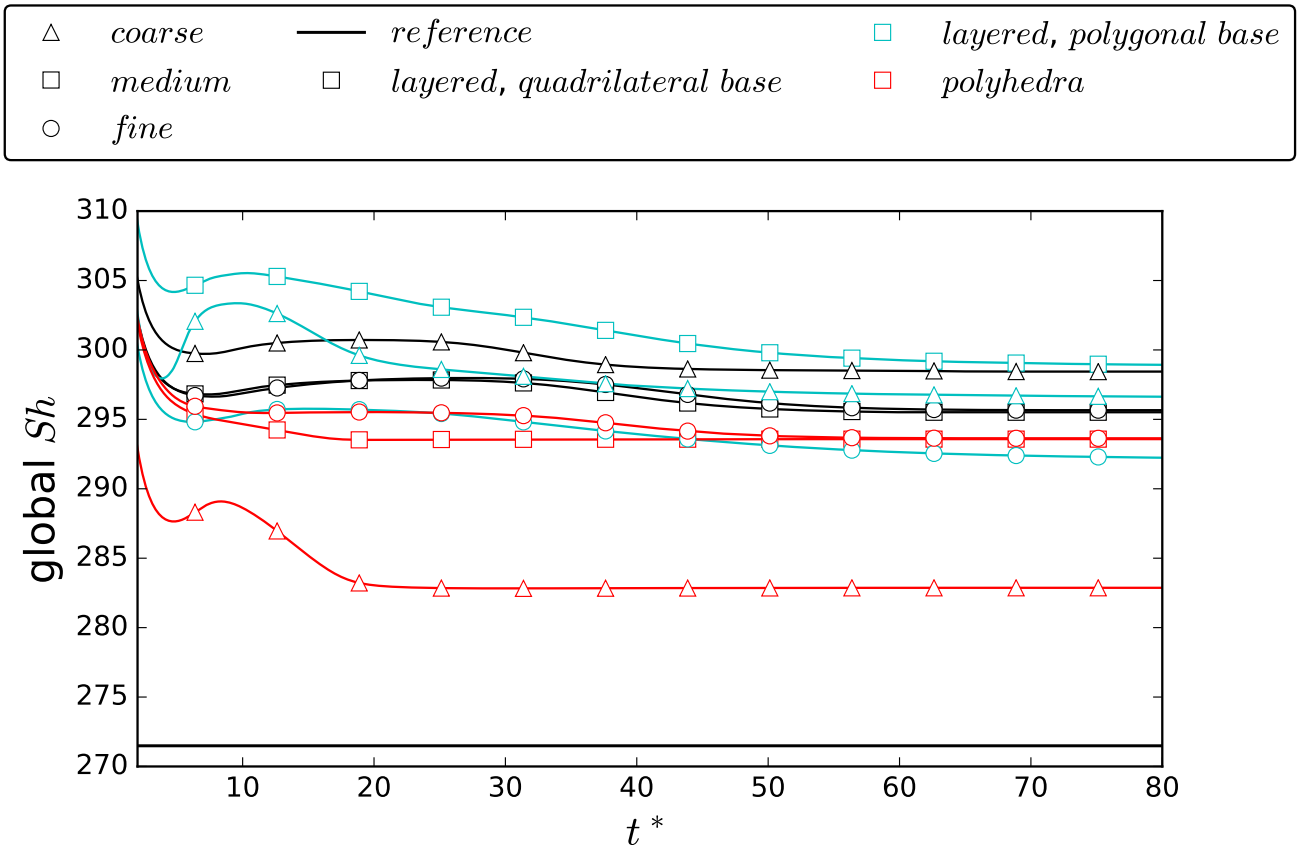

Figure 5.9: Enlarged excerpt with the global Sherwood numbers of the layered meshes and the polyhedra mesh.

for those strategies (see Table 5.2) and the layer formation is robust and even. As mentioned before, the velocity field at the outer domain boundaries of the hexahedron-dominated meshes is not homogeneous. This problem is investigated in subsection 5.1.7.

The *medium* layered mesh with quadrilateral base is tested again with lower tolerances for velocity and pressure solution (Table 5.5) to study the behaviour of the solver and potential influences on the solution. In fact, the solutions for pressure and velocity field do not reach a steady state with this setup. However, the result does not change at all.

Parameter	Solver	Adjusted Tolerance
A	`PBiCGStab`	$1 \cdot 10^{-9}$
p	`GAMG`	$1 \cdot 10^{-9}$
U	`smoothSolver`	$1 \cdot 10^{-12}$

Table 5.5: Solvers and adjusted tolerances.

5.1.3 Scale of segregation

The change of the inverse length scale φ is analyzed at $t^* = 62.5$. The results are extracted from all twelve meshes and summarized in Table 5.6.

For the layered mesh with quadrilateral base the expected result can be observed, i.e. φ rises with increasing mesh size. The rate of change between the *fine* and the *medium* mesh is lower than between the *medium* and

	Layered mesh with quadrilateral base	Hexahedron-dominated	Layered mesh with polygonal base	Polyhedron-dominated
coarse	443.3	425.8	436.9	450.1
medium	456.3 (+2.93 %)	605.2 (+42.1 %)	447.5 (+2.43 %)	434.3 (−3.51 %)
fine	464.2 (+1.73 %)	558.5 (−7.72 %)	458.9 (+2.55 %)	463.9 (+6.82 %)

Table 5.6: Calculated φ for all three mesh sizes of the four meshing strategies.

the *coarse* mesh, thus the value can be expected to converge. After the first mesh refinement of the hexahedron-dominated mesh, φ increases by about 42 %, but then decreases by almost 8 % for the *fine* mesh. Looking at the layered meshes with polygonal base, φ rises with increasing mesh size although the change of φ is higher between *fine* and *medium* mesh than between *medium* and *coarse* mesh. The tendencies of the polyhedra meshes are contrary to the hexahedron-dominated meshes. A decrease of φ between the *medium* and the *coarse* mesh is followed by an increase between the *fine* and the *medium* mesh. The results of the layered and the polyhedra meshes allow the assumption that the final value of φ for those mesh types may lie around 460 to 480 while the figures of the *medium* and *fine* hexahedron-dominated meshes are further away from that range which fits the observation of the global Sherwood numbers.
The development of φ for the hexahedron-dominated meshes is not even monotone, which can only be explained by the fact that each setup resolves the hydrodynamics differently. As species transport happens at a smaller scale than momentum transport for $Sc > 1$ (see chapter 1) statements about mesh convergence are only sensible if the velocity field does not change between two meshes. This counts for the polyhedra meshes although the boundary layer cells in the *medium* and *fine* polyhedra meshes are of the size estimated in chapter 1. Two reasons for this are conceivable. Firstly, the correlation from chapter 1 can overestimate the actual thickness of the boundary layer. Secondly, besides the boundary layer the influence of the wake resolution on the results must be considered.

Mesh size of the hexahedron-dominated meshes

The global Sherwood numbers of the hexahedron-dominated meshes differ qualitatively and quantitatively. To further examine the evolution of the results, hexahedron-dominated meshes with more cells are tested. This time, only the background mesh of the *fine* hexahedron mesh is manipulated such that meshes with $1.6 \cdot 10^6$, $3.2 \cdot 10^6$, $4.1 \cdot 10^6$ and $5.0 \cdot 10^6$ are created. All other meshing parameters are kept constant. The results of the meshes with $4.1 \cdot 10^6$ and $5.0 \cdot 10^6$ cells are unstable and do not match the expectations. Some statistics of the new meshes are summarized in Table 5.7. In Table 5.8 the cell sizes of the cells in the wake and the integral scale of segregation in the different hexahedron-dominated meshes are compared. This is important with regard to (4.3) and the Batchelor scale. The global Sherwood numbers of all five differently sized hexahedron-dominated meshes are reported in Figure 5.10.
The trends of the two added mesh sizes lie between those of the *medium* and *fine* mesh, which means the discrepancy between the results and the reference solution is higher for the meshes with $1.6 \cdot 10^6$ and $3.2 \cdot 10^6$ cells than for the *fine* mesh. At the same time, the extent of the local minimum before $t^* = 10$ reduces. In fact, the mesh with $3.2 \cdot 10^6$ cells shows the straightest trend of all hexahedron-dominated meshes. The values of φ for the meshes with $1.6 \cdot 10^6$ and $3.2 \cdot 10^6$ cells increase but with a decreasing rate of change.

	$1.6 \cdot 10^6$ **cells**	$3.2 \cdot 10^6$ **cells**
Mesh size	1 580 344	3 251 381
Maximum skewness	0.5717	0.6585
Maximum/average non-orthogonality	41.78/2.503	42.06/2.214
Thickness of the first/ first five cell(s) in radial direction	6.5 μm/34.2 μm	4.9 μm/26.6 μm
Time increment/ maximum Co at the beginning	$2.5 \cdot 10^{-5}$/0.5315	$2 \cdot 10^{-5}$/0.5881

Table 5.7: Mesh statistics of the hexahedron-dominated meshes with $1.6 \cdot 10^6$ and $3.2 \cdot 10^6$ cells.

	coarse	***medium***	***fine***	$1.6 \cdot 10^6$ **cells**	$3.2 \cdot 10^6$ **cells**
Cell size in the wake	98 μm	76 μm	60 μm	47 μm	37 μm
φ	425.8	605.2 (+42.1 %)	558.5 (−7.72 %)	660.6 (+18.3 %)	752.3 (+13.9 %)

Table 5.8: Cell sizes in the wake and values of φ in the hexahedron-dominated meshes.

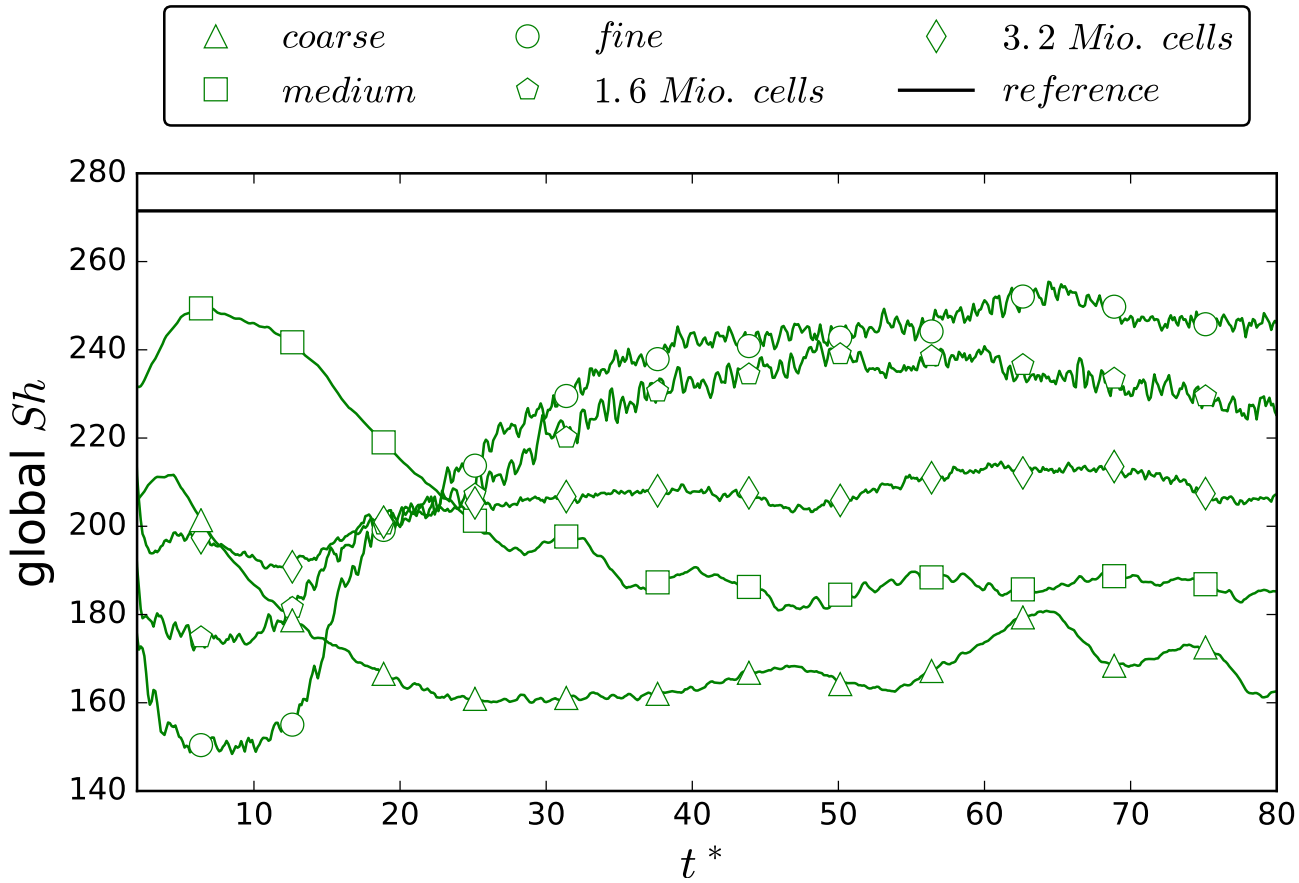

Figure 5.10: Global Sherwood numbers of the hexahedron-dominated meshes with five different numbers of cells.

5.1.4 Concentration fields and streamline plots

Concentration fields

The concentration fields of the *coarse*, *medium* and *fine* meshes are shown in Figure 5.11 to Figure 5.14. The results of the two additional hexahedron-dominated meshes are reported, too. The snap shots are all taken at the same dimensionless time $t^* = 62.5$, which equals $t = t^* \cdot d_b/U_b = 62.5 \cdot 2 \cdot 10^{-3}\,\mathrm{m}/2.5 \cdot 10^{-1}\,\mathrm{m\,s^{-1}} = 0.5\,\mathrm{s}$ of physical time in the case of $Re = 500$.

In all three layered meshes with quadrilateral base the species is concentrated in a closed wake that broadens with greater distance to the bubble. The size of the wake reduces with increasing mesh size. The highest concentrations are found at the lower side of the bubble in a ring around the south pole. The radius of the concentration ring stays constant. The concentration inside the ring below the south pole is higher in the *medium* mesh than in the *coarse* mesh. For the *fine* mesh, a third concentration peak forms right below the south pole.

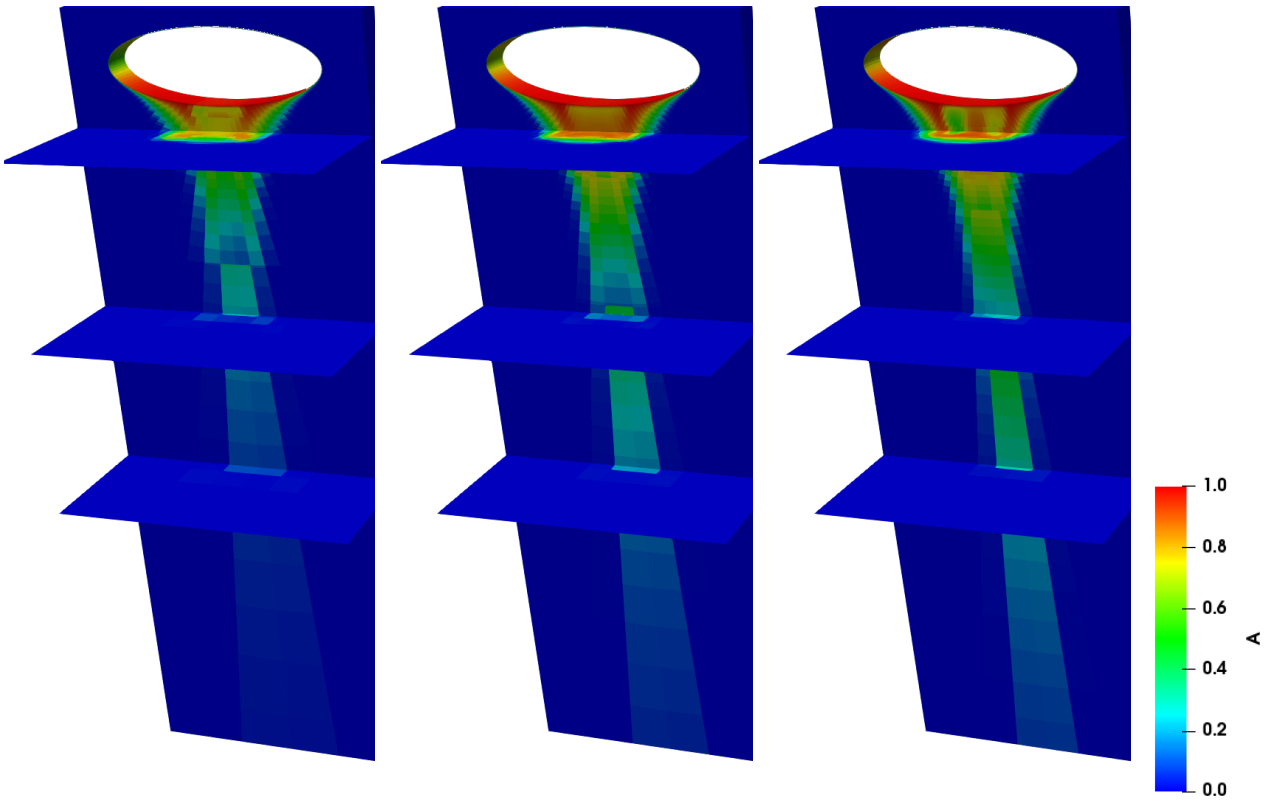

(a) *coarse* **(b)** *medium* **(c)** *fine*

Figure 5.11: Concentration fields of the layered meshes with quadrilateral base at $t^* = 62.5$.

Looking at the concentration fields of the hexahedron-dominated meshes it is noticeable that the concentration does not form a closed wake, but seperates in a thin ring around the bubble's south pole that can be seen on the top level cross-section plane. The *fine* mesh has the narrowest concentration ring. In the *coarse* case, the species concentration in the wake is the lowest. Moreover, vortical structures can be identified, indicating an instationary flow pattern. Additionally, in the *fine* mesh a second concentration ring inside the first ring is clearly visible. Apart from the ring, the concentration fields of the four finer meshes look very different from each other. This confirms the observation that the results are still dependent from the mesh because for each mesh, different solutions for the velocity field are calculated.

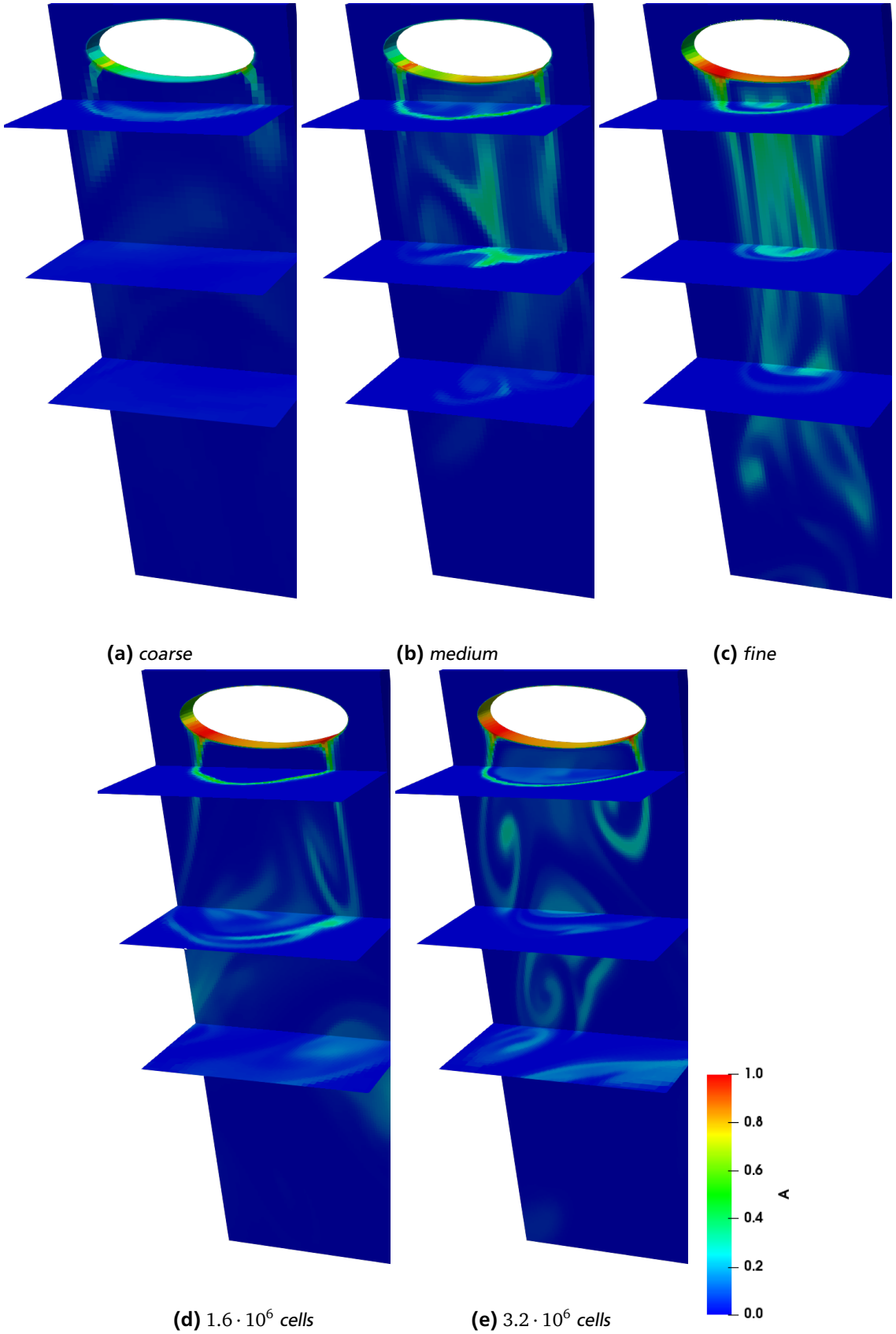

(a) *coarse* **(b)** *medium* **(c)** *fine*

(d) $1.6 \cdot 10^6$ *cells* **(e)** $3.2 \cdot 10^6$ *cells*

Figure 5.12: Concentration fields of the hexahedron-dominated meshes at $t^* = 62.5$.

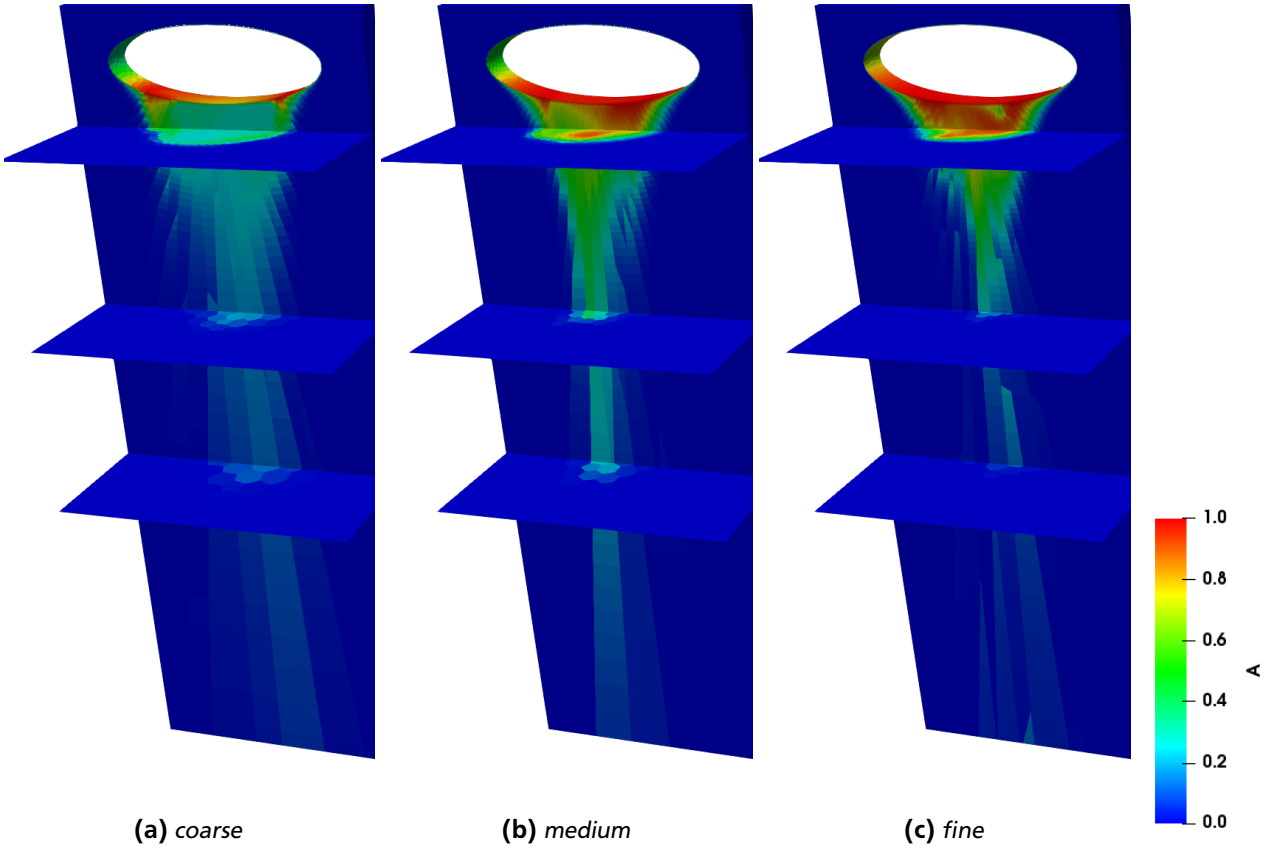

(a) *coarse* **(b)** *medium* **(c)** *fine*

Figure 5.13: Concentration fields of the layered meshes with polygonal base at $t^* = 62.5$.

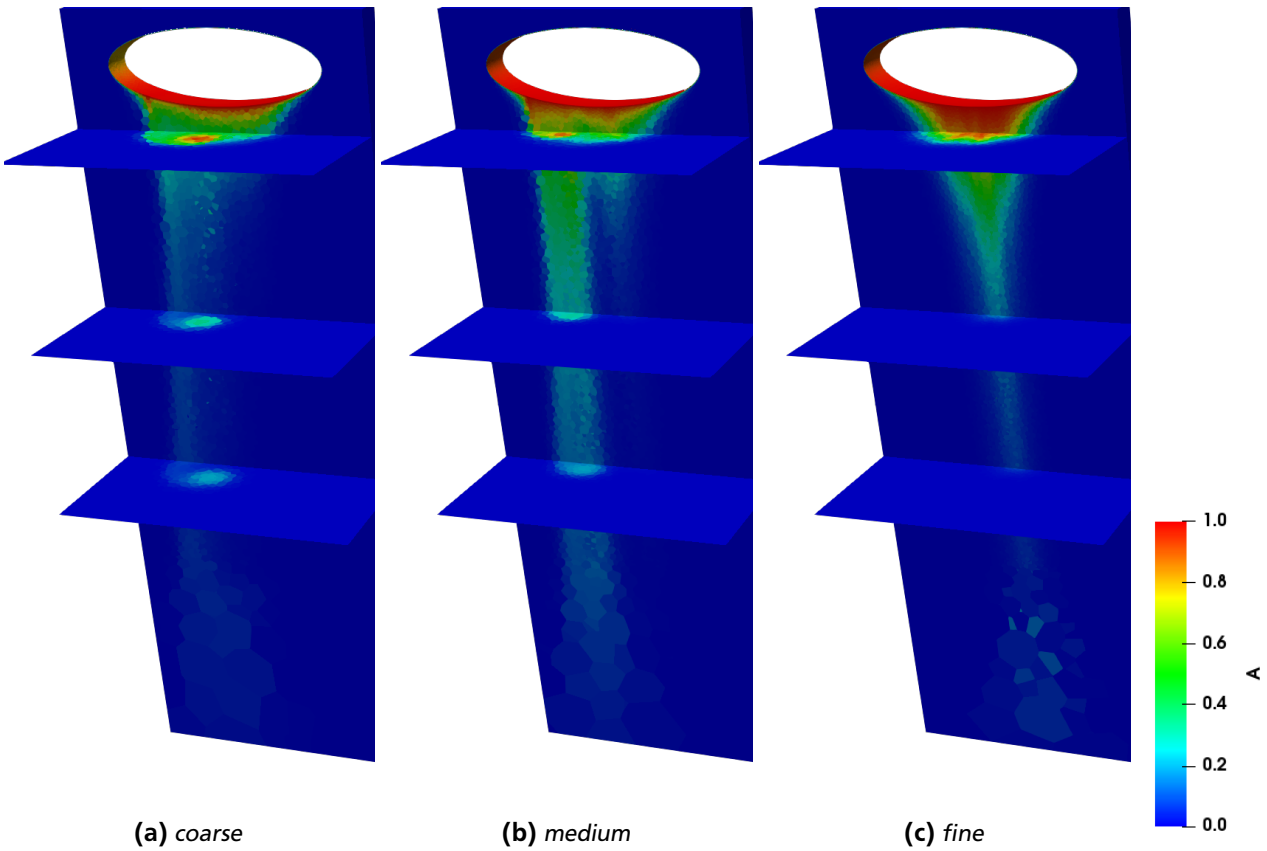

(a) *coarse* **(b)** *medium* **(c)** *fine*

Figure 5.14: Concentration fields of the polyhedra meshes at $t^* = 62.5$.

Similarly to the layered meshes with quadrilateral base, the concentration of the layered meshes with polygonal base show a closed concentration wake that broadens and frays with greater distance to the bubble. In the *coarse* mesh signs of a concentration ring around the lower side of the bubble is detectable. The ring is found in the finer meshes, too, but inside, around the south pole, the concentration is higher.

In the *coarse* and *medium* cases of the polyhedra meshes the wake runs a little shifted from the middle and in the *medium* mesh a second smaller wake is present. The wake of the *coarse* mesh is twisted, which might be an indication for vorticity in the flow. In the *fine* mesh one narrowing tube is seen that broadens when the concentration leaves the refinement box.

Streamline plots

For the *coarse*, *medium* and *fine* meshes of each meshing strategy the streamline plots at $t^* = 62.5$ are shown in Figure 5.15 to Figure 5.18. The results of the additionally refined hexahedron-dominated meshes are reported, too. In the streamline plots of the layered and the polyhedra meshes recirculations are absent. Only weak signs of vorticity are detectable. Differences between the differently sized meshes are small but present, which shows that the resolution of the hydrodynamics is still mesh sensitive. The streamline plots of the hexahedron-dominated meshes are different from the other meshing strategies. All five meshes show an unsteady three-dimensional wake but with significant variations amongst themselves.

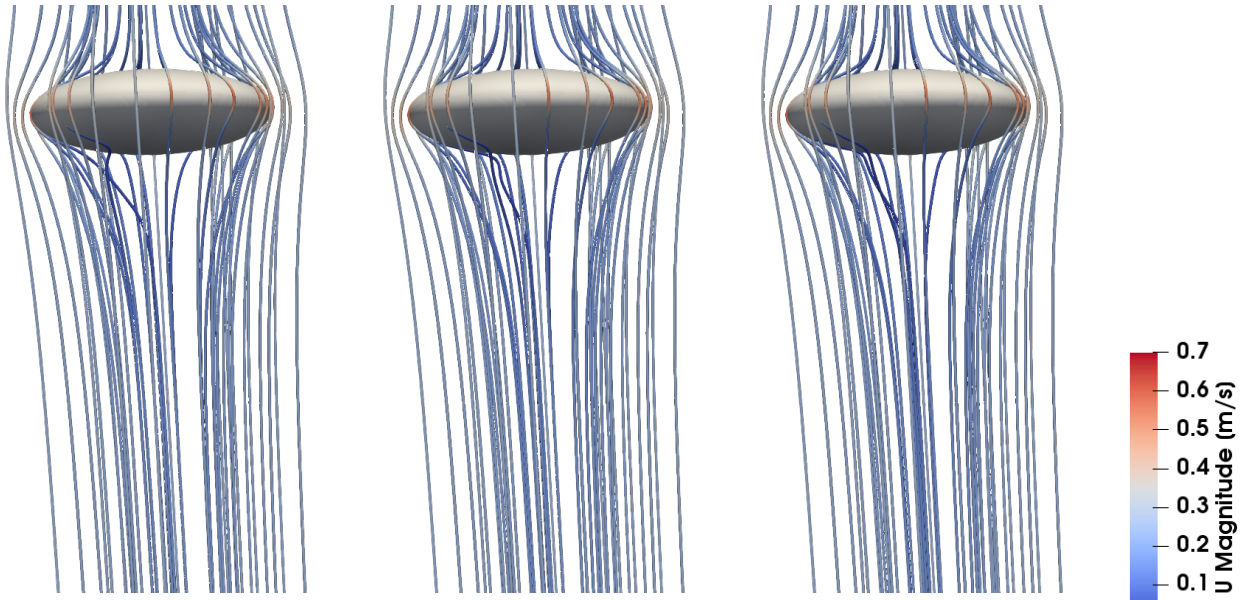

(a) *coarse* **(b)** *medium* **(c)** *fine*

Figure 5.15: Streamline plots of the layered meshes with quadrilateral base at $t^* = 62.5$.

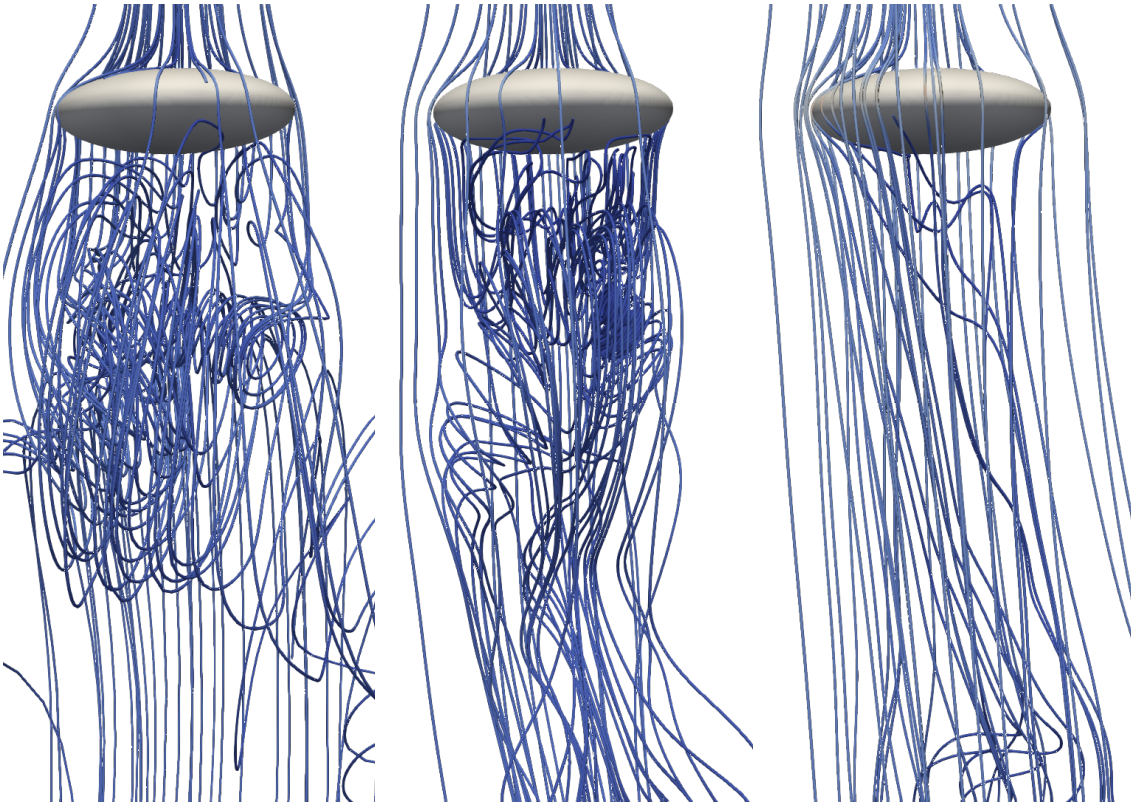

(a) *coarse* **(b)** *medium* **(c)** *fine*

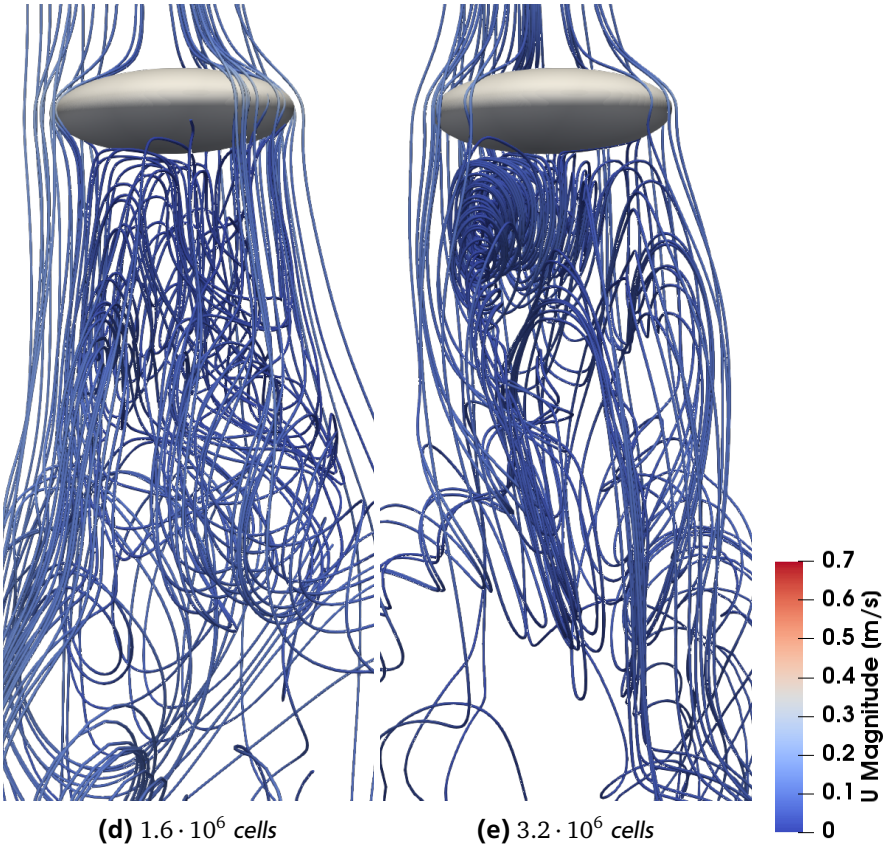

(d) $1.6 \cdot 10^6$ *cells* **(e)** $3.2 \cdot 10^6$ *cells*

Figure 5.16: Streamline plots of the hexahedron-dominated meshes at $t^* = 62.5$.

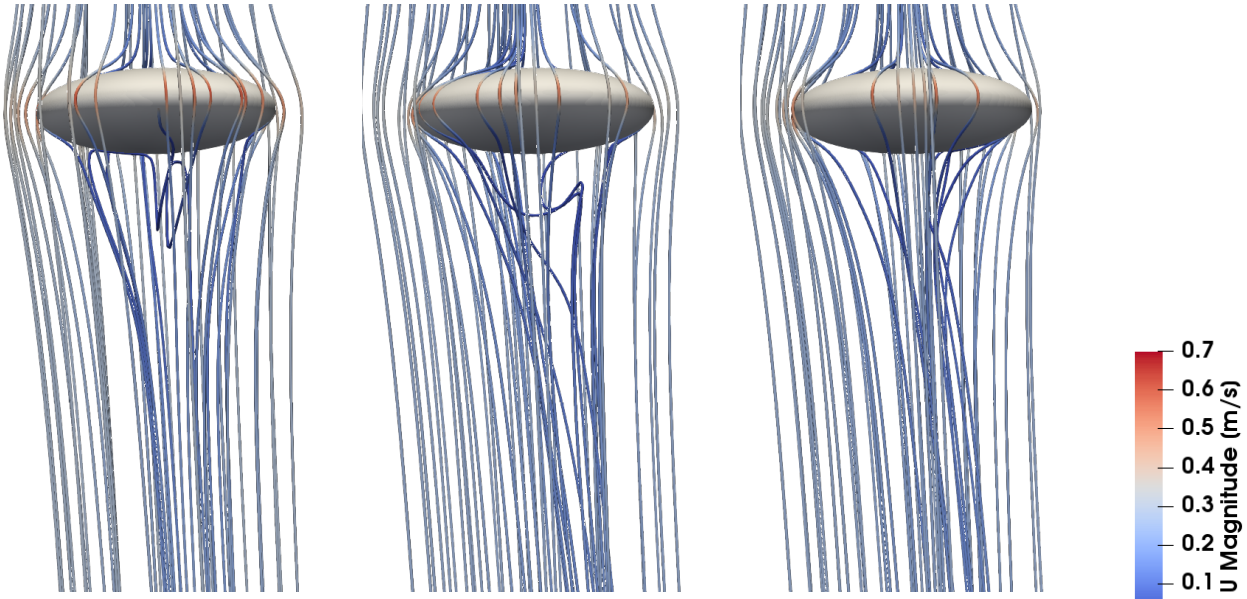

(a) *coarse* **(b)** *medium* **(c)** *fine*

Figure 5.17: Streamline plots of the layered meshes with polygonal base at $t^* = 62.5$.

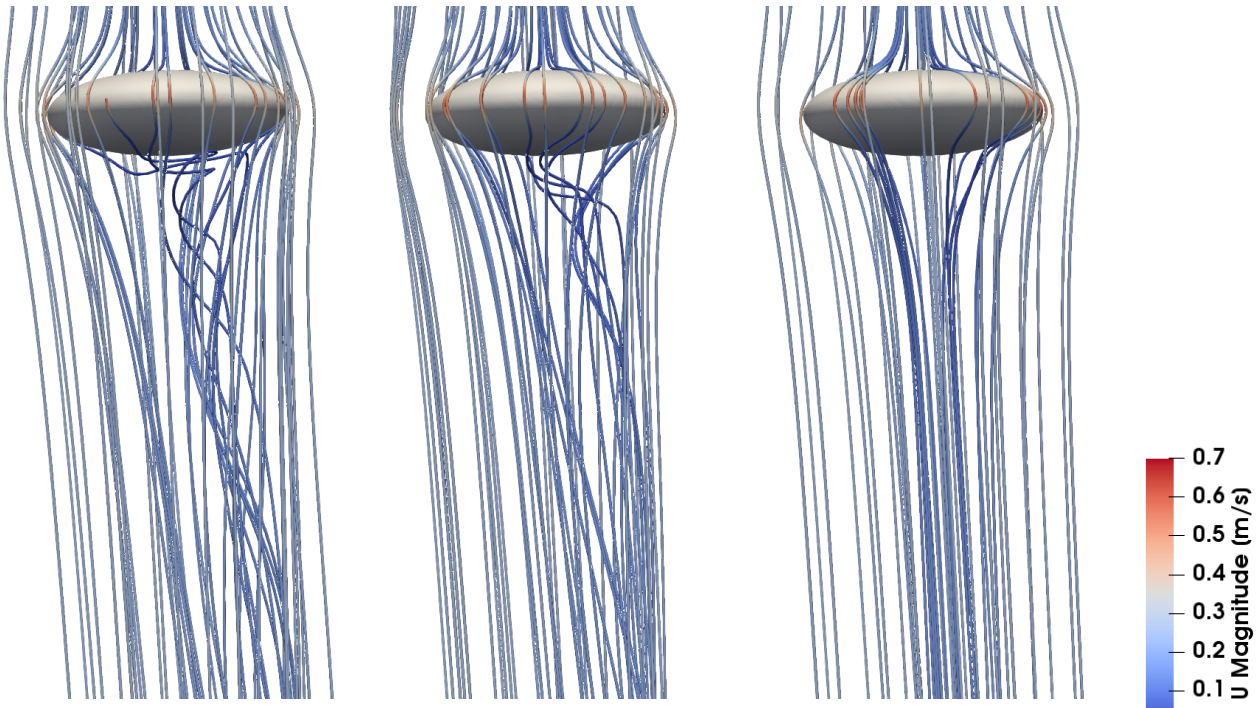

(a) *coarse* **(b)** *medium* **(c)** *fine*

Figure 5.18: Streamline plots of the polyhedra meshes at $t^* = 62.5$.

5.1.5 Size of the refinement region

The evaluation of the results from the *hexahedron-dominated* meshes show that the diameter of the refinement cylinder does not cover all traces of concentration. The influence of the size of the refinement region on the global Sherwood number is studied by varying the cylinder radius in the *medium* mesh. In the original setup the radius is 2 mm. Refinement boxes with radii of 1.5 mm, 2.5 mm, 3.0 mm and 4.0 mm are taken into account for comparison. The choice is based on the visual evaluation of the original set up which means that the largest diameter covers all areas where a concentration of the transfer species A is observed. The smallest and the largest refinement regions are compared in Figure 5.19. The global Sherwood numbers are depicted in Figure 5.20. To quantify the influence of the refinement region size the global Sherwood numbers are averaged from $t^* = 30$ to $t^* = 80$.

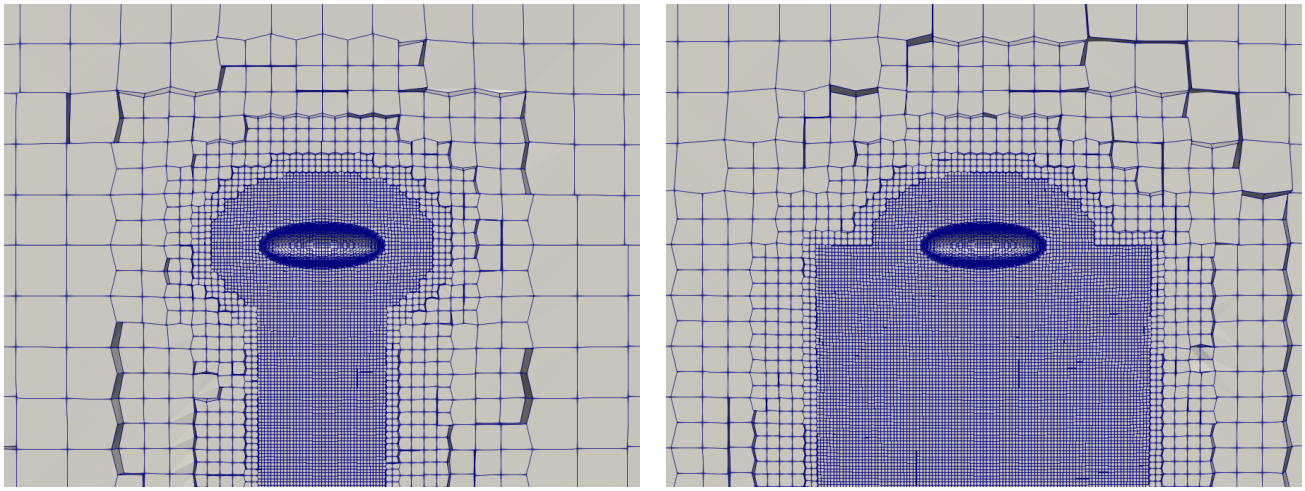

(a) *smallest* **(b)** *largest*

Figure 5.19: Smallest and largest refinement regions in the wake study of the hexahedron-dominated mesh.

	1.5 mm	2 mm	2.5 mm	3 mm	4 mm
Mean equivalent global Sh	188.67	187.31	192.98	191.86	189.83
φ	567.45	605.2	550.2	572.5	570.0

Table 5.9: Averaged global Sherwood numbers from $t^* = 30$ to $t^* = 80$ and values of φ at $t^* = 62.5$ of the *medium* hexahedron-dominated meshes with differently sized wake refinement regions.

In this specific setup the changes caused by increasing the refinement region size can be neglected. Even a smaller refinement region brings a comparable result. However, in setups with more cells this might be different as the wake in the other hexahedron-dominated meshes has a different shape.

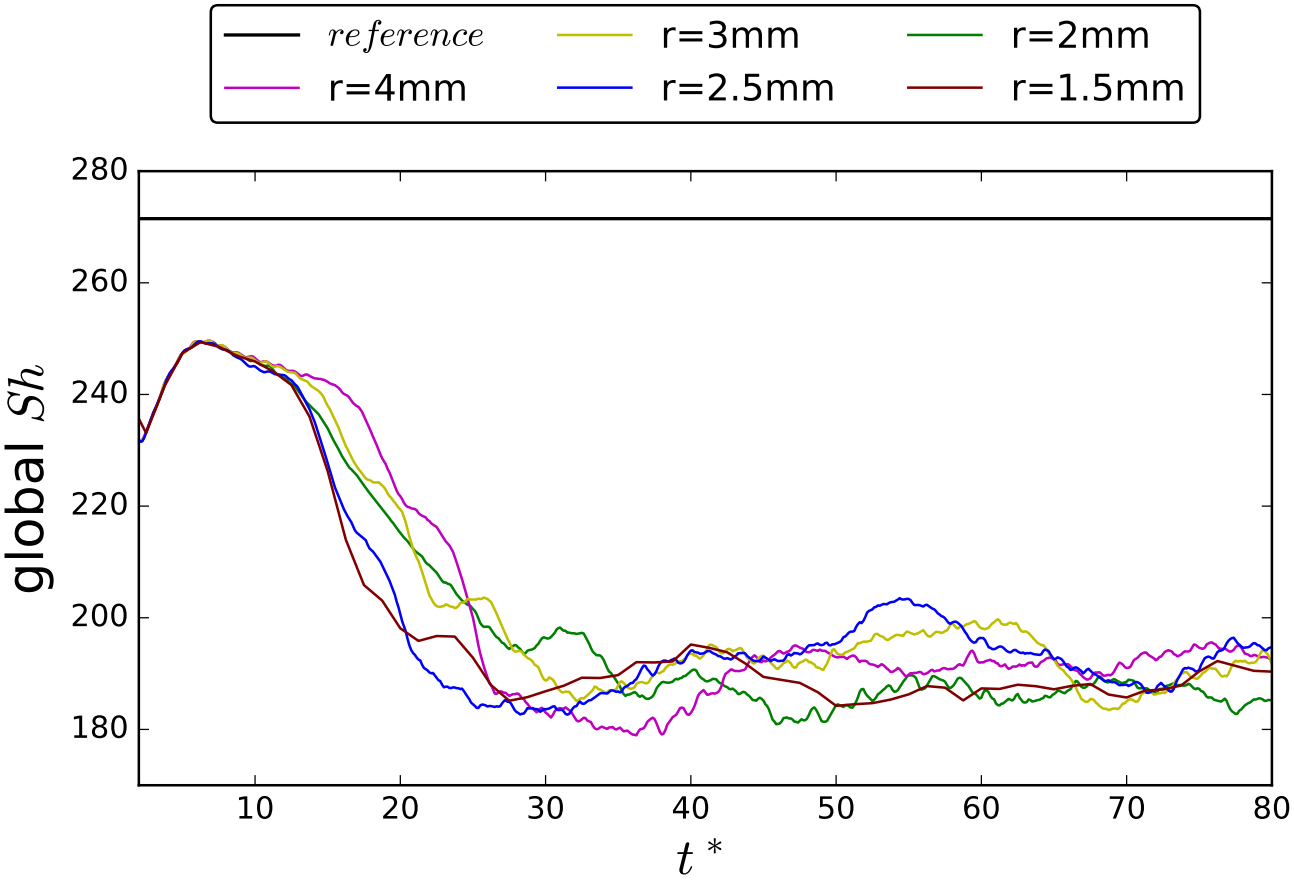

Figure 5.20: Global Sherwood numbers of the hexahedron-dominated meshes with differently sized wake refinement regions.

5.1.6 Surface mesh of the hexahedron-dominated meshes

The reasons why the hexahedron-dominated meshes resolve the hydrodynamics differently than the other meshing strategies are further examined. The originally used hexahedron-dominated setups have fewer faces on the interface than the other meshing strategies. The number of faces on the interface dictates the quality of the shape representation and can be decisive whether flow seperation appears or not. The numbers of faces are summarized in Table 5.10. Figure 5.21 demonstrates that the surface representation of the *coarse* hexahedron-dominated mesh is not very good.

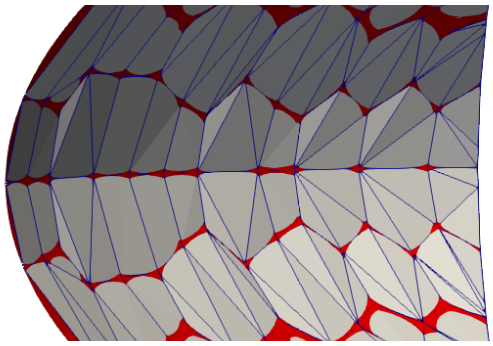

Figure 5.21: Surface representation at the equator of the *coarse* hexahedron-dominated mesh.

	Layered mesh with quadrilateral base	Hexahedron-dominated	Layered mesh with polygonal base	Polyhedron-dominated
coarse	3610	1560	2899	7099
medium	5664	2512	4630	23 937
fine	9000	4128	7080	30 275

Table 5.10: Numbers of faces on the interface.

The *coarse* and *fine* hexahedron-dominated meshes are tested again but the surface refinement level is raised by 1 in both setups. This results in both meshes now having four times as many cells on the surface. The overall cell numbers change to 251 722 and 932 584. Now, the global Sherwood numbers and the residuals for the new setups are compared to the original *coarse* and *fine* hexahedron-dominated meshes. `SnappyHexMesh` automatically creates a refinement level grading if surface and surrounding mesh do not have the same refinement level. Incidentally, this seems to be a method for reaching smaller boundary layer cell thicknesses without significantly increasing the cell size. In Figure 5.22 the global Sherwood numbers for the coarse and fine meshes are compared to the solutions with finer surface meshes. The changes of the inverse length scale φ are evaluated like in Table 5.6 and compared in Table 5.11. Note that the results with the refined surface meshes show less perturbations because the numbers of solutions are decimated in those setups due to the more efficient usage of storage capacity.

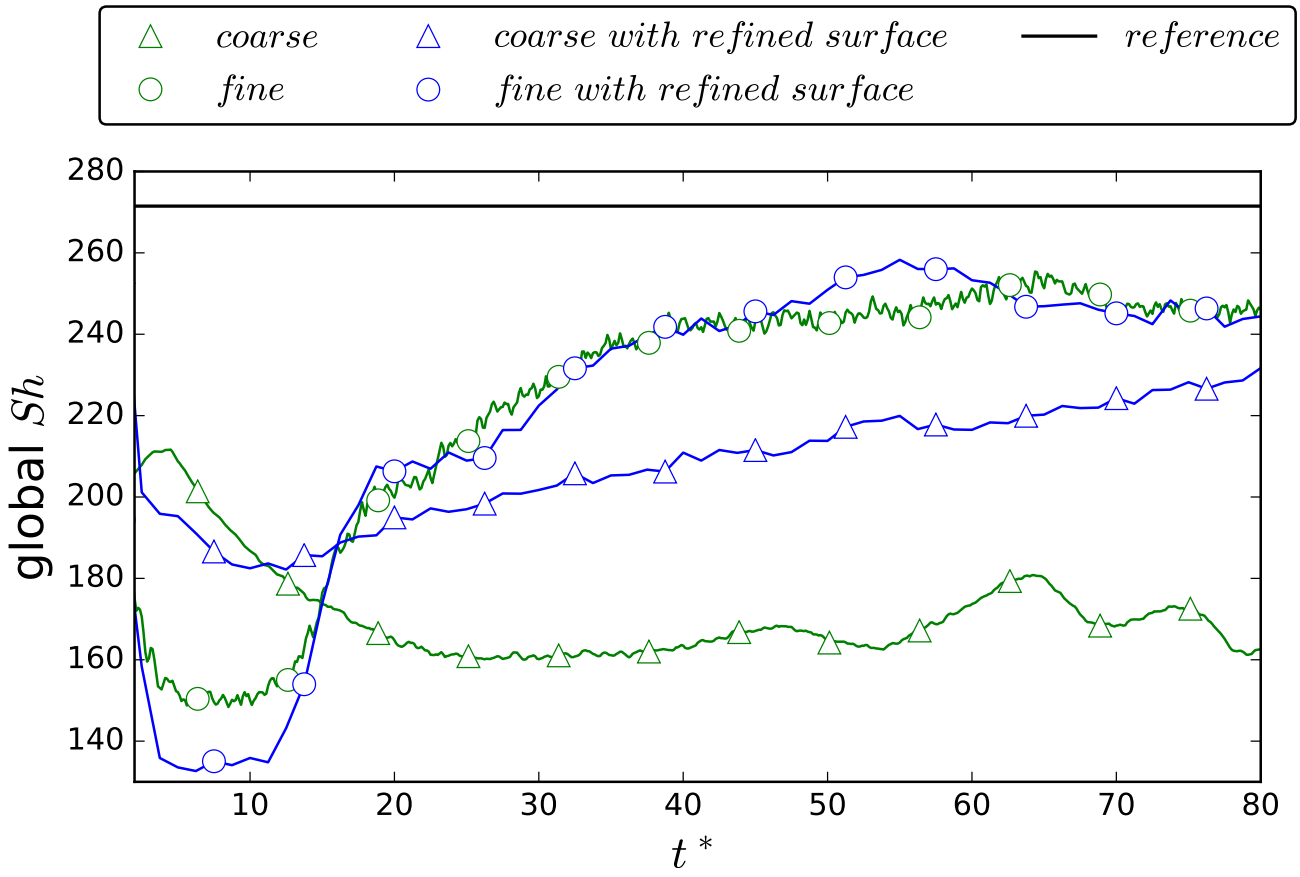

Figure 5.22: Global Sherwood numbers of the *coarse* and *fine* hexahedron-dominated meshes with different surface mesh resolutions.

	Old surface mesh	New surface mesh
coarse	425.8	524.6 (+23.2 %)
fine	558.5	524.3 (−6.12 %)

Table 5.11: φ of the *coarse* and *fine* hexahedron-dominated meshes with differently fine surface meshes.

5.1.7 Oscillations in the velocity field of the hexahedron meshes

At the outer domain boundary of the hexahedron domianted meshes oscillations of the velocity field are present, see Figure 5.23, although no instabilities should be present here. This influences the results around the bubble and can be an explanation for the unexpected results of the hexahedron-dominated meshes compared to the other meshing strategies.

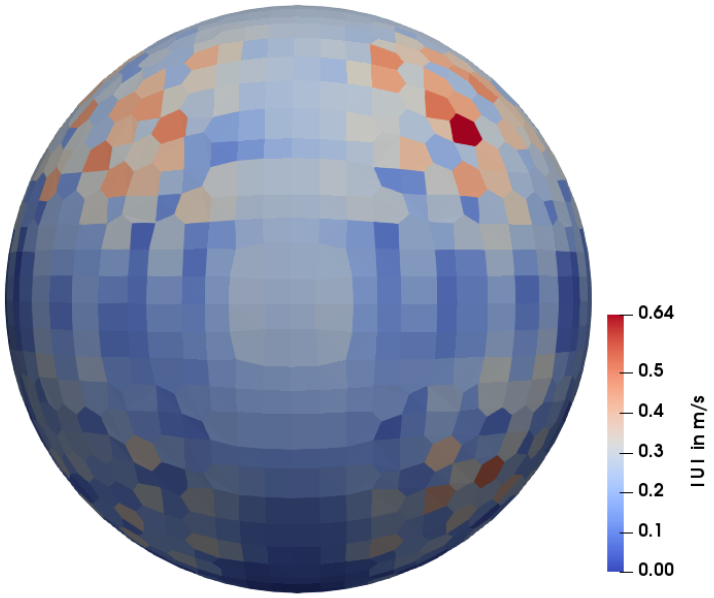

Figure 5.23: Oscillations in the velocity field at the outer domain boundary of the hexahedron mesh.

The addition of layers at the outer domain boundary can solve this problem, as shown in Figure 5.24.

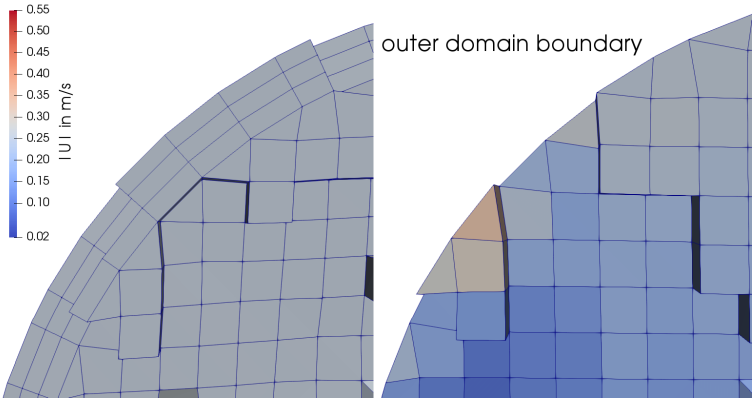

Figure 5.24: Velocity field at the outer domain boundary of the hexahedron dominated mesh; with and without layers.

5.2 Variation of key parameters

To observe different flow regimes, the Reynolds number is varied. Figure 1.2 indicates that for a bubble with aspect ratio $\chi = 3$ and a Reynolds number of 50 axisymmetric recirucaltions are to be expected. The Schmidt number is varied between 10 and 100. In Figure 5.26, the concentration fields of the setups with varying Reynolds and Schmidt numbers are compared. The *fine* hexahedron-dominated mesh is used.

The most significant difference between the concentration fields with the same Reynolds number but a different Schmidt number is that with the lower Schmidt number the species is more spread. This is because with a lower Peclet number the significance of diffusion rises compared to convection. Moreover, on the bottom level plane the coarse resolution suggests that calculating lower Reynolds numbers requires a larger refinement box.

In Figure 5.25, the streamline plots for $Re = 50$ and $Re = 500$ at $t^* = 37.5$ are compared. Note that the scale of the snapshot with $Re = 50$ ranges from $0\,\mathrm{m\,s^{-1}}$ to $0.07\,\mathrm{m\,s^{-1}}$.

The reconstruction of the expected flow patterns fails. For $Re = 50$, the wake structure is still unstable and not an axisymmetric recirculation. Setups with $Re = 5$ are carried out, too, but the results are inaccurate. This problem can probably be solved with the layers around the outer domain boundary, see Figure 5.24.

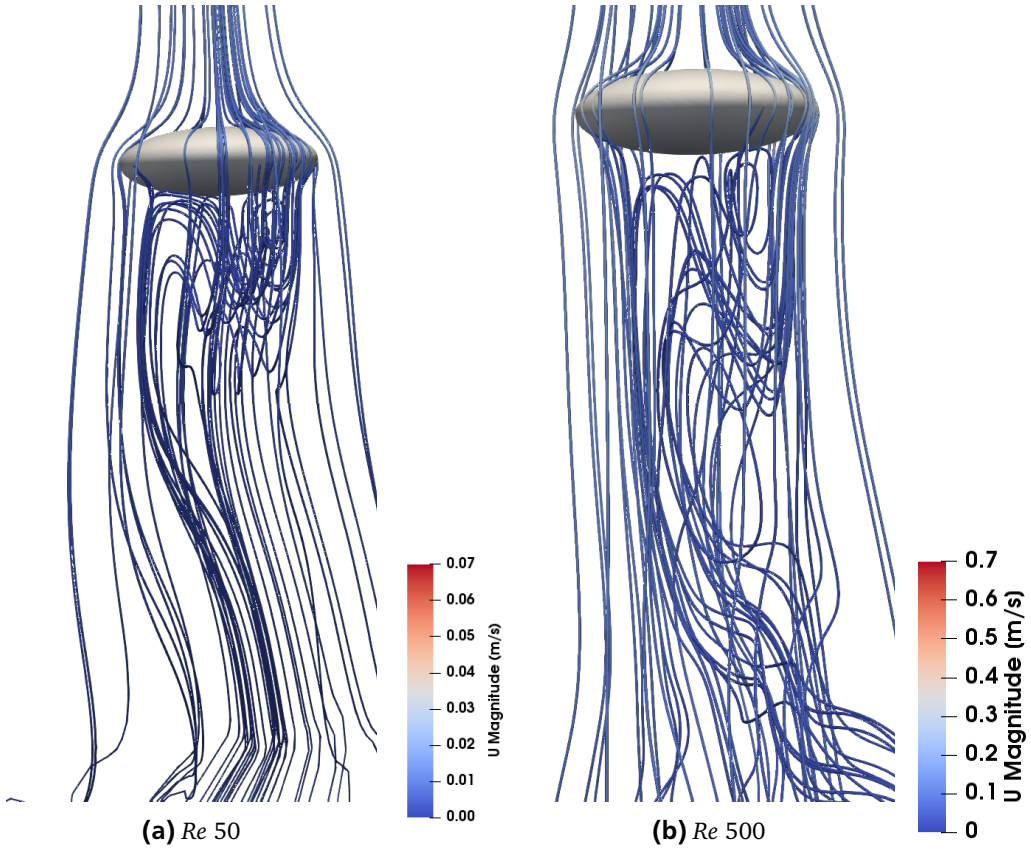

(a) *Re* 50 **(b)** *Re* 500

Figure 5.25: Streamline fields of the *fine* hexahedron-dominated mesh with $Re = 50$ and $Re = 500$ at $t^* = 37.5$.

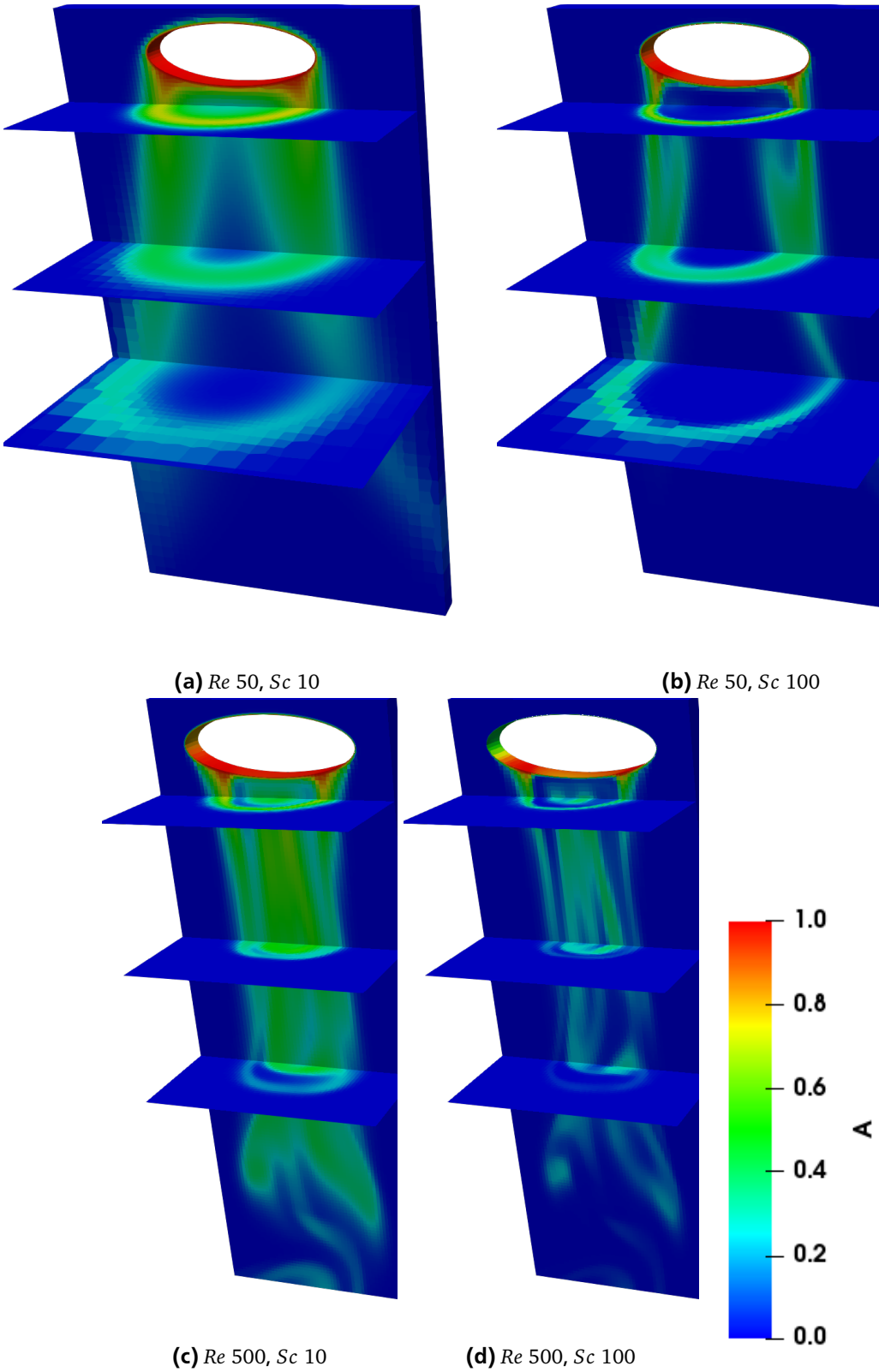

(a) Re 50, Sc 10 **(b)** Re 50, Sc 100

(c) Re 500, Sc 10 **(d)** Re 500, Sc 100

Figure 5.26: Concentration fields of the *fine* hexahedron-dominated meshes with varying Reynold and Schmidt numbers at $t^* = 62.5$.

5.3 Run- and CPU-time

The necessary CPU-time is compared by means of another set of cases that all have the same time increment and run for the same amount of iterations. The time performance computations are each run on a single node of the cluster that is only processing this specific setup at the time. For a reasonable comparison the setups have the same time increment of $5 \cdot 10^{-6}$ s, so all meshes start with a maximum Courant number < 1. The end time is set to $5 \cdot 10^{-3}$ s such that 1000 iterations are carried out. In Figure 5.27 the run-time and the CPU-time of all tested setups are presented.

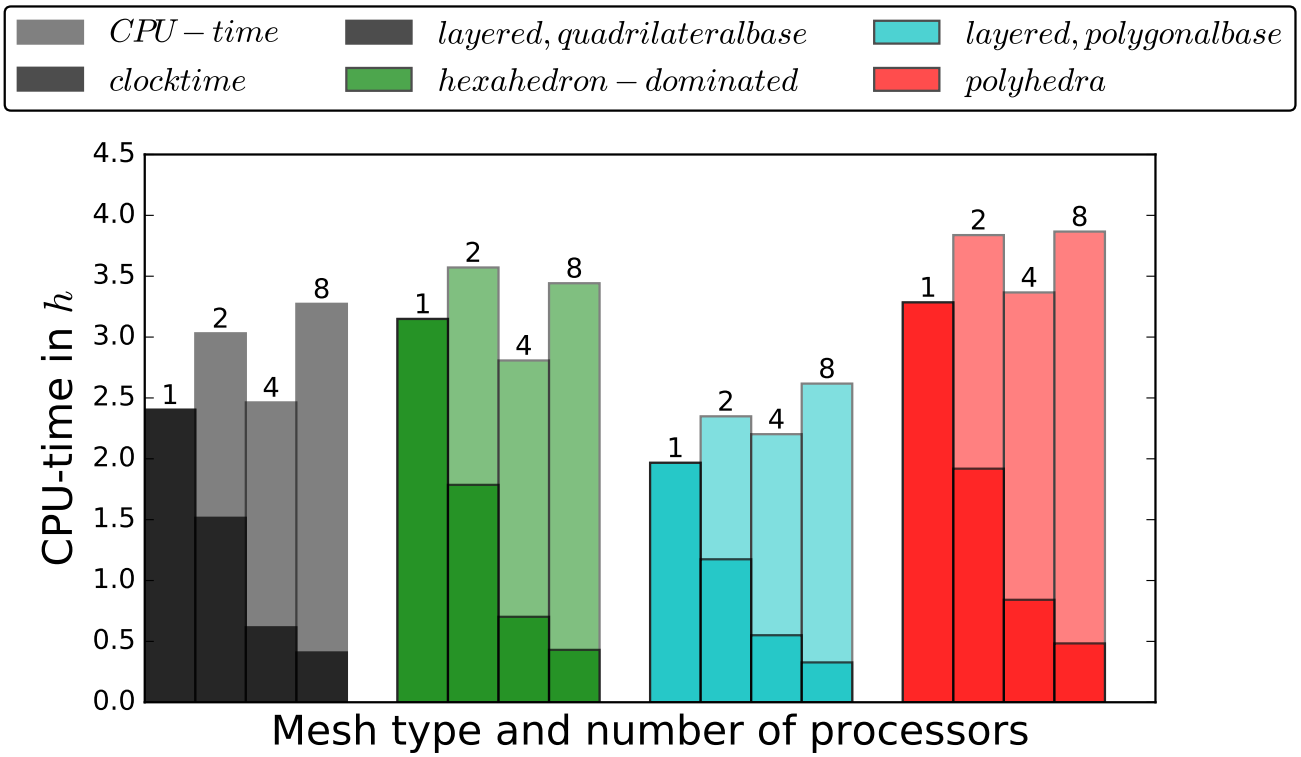

Figure 5.27: Required run- and CPU-time.

Independent from the number of processors, the layered mesh with polygonal base is the fastest, followed by the layered mesh with quadrilateral base, the hexahedron-dominated mesh and the polyhedra mesh. As expected, using more processors reduces the run-time in all setups. The scaling between CPU-time and number of processors is evaluated in Table 5.12 by comparing the run-time with one processor to the run-time with two, four and eight processors.

	Layered mesh with quadrilateral base	**Hexahedron-dominated**	**Layered mesh with polygonal base**	**Polyhedron-dominated**
Two processors	63 %	57 %	60 %	58 %
Four processors	26 %	22 %	28 %	26 %
Eight processors	17 %	14 %	17 %	15 %

Table 5.12: Run-time of the decomposed cases compared to the case on one processor.

Remarkable is that for all four meshing strategies the CPU-time with four processors is lower than with two processors and in the case of the hexahedron-dominated mesh even lower than in the setup with only one processor. Usually, it would be expected that doubling the number of processors does not quite halve the run-time of the computation. That is because with an increasing number of processors the necessary clocktime for communication between them also rises. This way it can be explained why the setups with two processors need more CPU-time than the setups with one processor. The same goes for the fact that the setups with eight processors need the most CPU-time, although this is not true for the hexahedron-dominated mesh.
However, the time a computation needs is also influenced by other parameters like the number of solver iterations for the solution of velocity, pressure and concentration field. The `GAMG` solver calculates six solutions for the pressure p. In Table 5.13 the averaged numbers of pressure iterations are reported for all time performance setups to evaluate whether the number of iterations could explain the results from Figure 5.27.

	Layered mesh with quadrilateral base	**Hexahedron-dominated**	**Layered mesh with polygonal base**	**Polyhedron-dominated**
One processor	6.757	7.361	3.414	2.698
Two processors	7.536	7.677	3.520	2.719
Four processors	6.879	6.870	3.785	2.722
Eight processors	7.489	7.214	3.685	2.731

Table 5.13: Averaged numbers of iterations needed for the solution of p.

Only in the setups with the hexahedron-dominated mesh the ratios between the averaged numbers of iterations qualitatively match the results from Figure 5.27.
Presumably, the CPU-time is also influenced by the skewness and the average number of faces the cells have. The more faces a cell shares with neighbouring cells (see Table 5.2), the longer the calculations take, which could be why the polyhedra mesh needs the most CPU-time although the lowest number of iterations is executed.
Moreover, the decomposition of the domain by the `scotch` algorithm might have an influence on the parallel performance. As the decomposition takes place before the computation, the algorithm can only take the number of cells and the faces between the subdomains as criteria for an optimized decomposition. It is not taken into account that in the parts of the domain with steep gradients of pressure, velocity and species concentration, more iterations are necessary, so the solver needs more time. This could lead to the fact that the subdomains in the periphery have to wait for the ones in the vicinity and the wake of the bubble. The decomposition of the hexahedron-dominated mesh into two, four and eight subdmains is visualized in Figure 5.28.

For a further evaluation of the decomposition, the average and maximum number of cells and faces per processor during the time performance study are summarized in Table 5.14 to Table 5.17. The distributions of cells on the processors is homogeneous in all setups. The highest deviation of maximum from average cell number is 1 %. More striking is firstly the discrepancy in the number of faces for the setups with four and eight processors. Secondly, average and maximum numbers of faces in the layered mesh with polygonal base and in the polyhedra mesh are higher for four processors than for two and eight processors. For the hexahedron-dominated meshes, the setup with four processors has the highest maximum number of faces with the deviation of almost 50 % from the average value.

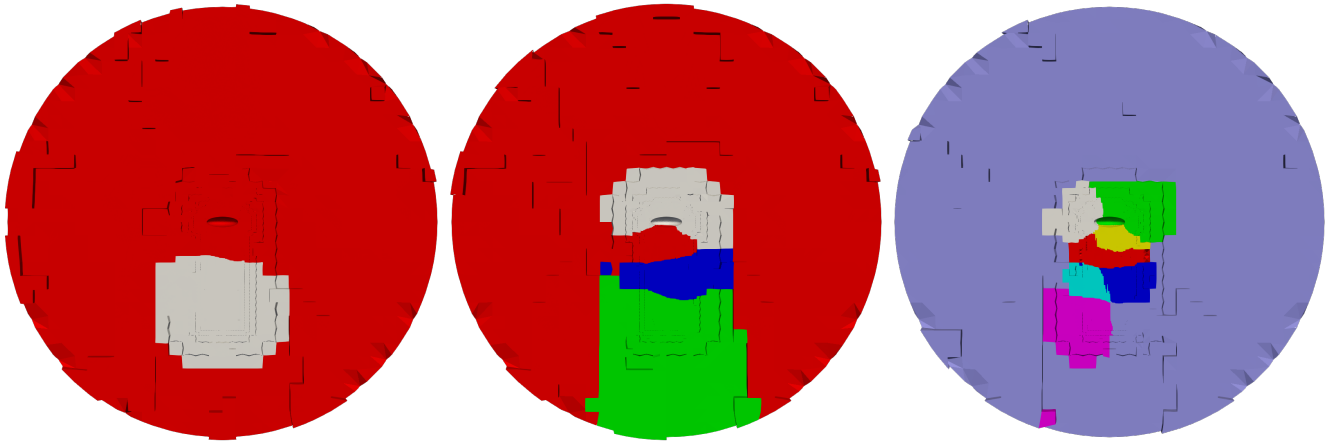

(a) Two processors **(b)** Four processors **(c)** Eight processors

Figure 5.28: Decomposition into subdomains.

	Two processors	Four processors	Eight processors
Average number of cells	203 904	101 952	50 976
Maximum number of cells (above average)	204 003 (+0.049 %)	102 587 (+0.62 %)	51 328 (+0.69 %)
Average number of faces	6382	7424	7598.5
Maximum number of faces (above average)	6382 (0 %)	7709 (+3.8 %)	8806 (+16 %)

Table 5.14: Processor statistics of the layered mesh with quadrilateral base.

	Two processors	Four processors	Eight processors
Average number of cells	207 347.5	103 672	51 859.5
Maximum number of cells (above average)	207 351 (0 %)	104 009 (+0.32 %)	52 375 (+0.98 %)
Average number of faces	4022	2738.8	1384.1
Maximum number of faces (above average)	4022 (0 %)	5390 (+49 %)	3295 (+59 %)

Table 5.15: Processor statistics of the hexahedron-dominated mesh.

	Two processors	Four processors	Eight processors
Average number of cells	203 720	101 860	50 930
Maximum number of cells (above average)	203 951 (+0.11 %)	102 718 (+0.84 %)	51 439 (+1.0 %)
Average number of faces	5139	10 160.5	9484.5
Maximum number of faces (above average)	5139 (0 %)	14 480 (+43 %)	11 265 (+19 %)

Table 5.16: Processor statistics of the layered mesh with polygonal base.

	Two processors	Four processors	Eight processors
Average number of cells	202 439.5	101 219.75	50 609.875
Maximum number of cells (above average)	202 651 (+0.10 %)	102 228 (+1.0 %)	51 115 (+1.0 %)
Average number of faces	17 220	18 490.5	14 840
Maximum number of faces (above average)	17 220 (0 %)	26 959 (+46 %)	20 947 (+41 %)

Table 5.17: Processor statistics of the polyhedra mesh.

6 Summary and Outlook

6.1 Summary

The procedure and the most important results are summarized in key points.

- Layered meshes with quadrilateral base are produced using the `blockMesh` utility from `OpenFOAM®`, hexahedron-dominated meshes are generated using the `snappyHexMesh` utility from `OpenFOAM®`. Layered meshes with polygonal base and polyhedra meshes are created using `salome®` and `OpenFOAM®`. Only hexahedron-dominated meshes can be created using parallel processing. In the hexahedron-dominated meshes and the polyhedra meshes refinement regions can be defined.

- The cell thickness in the boundary layer of the polyhedra mesh can be adjusted to any size. Limiting factor for the layered meshes is the cell aspect ratio. The thickness of the boundary layer cells in the hexahedron-dominated meshes is bound by internal mesh quality criteria of `snappyHexMesh`.

- Of each meshing strategy, meshes with 200 000, 400 000 and 800 000 cells are tested.

- The hexahedron-dominated meshes have the lowest maximum and average non-orthogonalities. The layered meshes with polygonal base have the highest occurring non-orthogonalities. Average and maximum skewness are highest in the polyhedra meshes. The layered meshes with polygonal base have the lowest maximum skewness. The distributions of non-orthogonality and skewness are similar for the different mesh resolutions of each strategy. The polyhedra meshes contain concave cells that are introduced by the creation oh the dual mesh via the `polyDualMesh` utility.

- The global Sherwood number is considered to evaluate the accuracy of the results. Most remarkable is the difference between the results of the hexahedron-dominated meshes and the other three meshing strategies. The reason for the differences is a different resolution of the hydrodynamics. This is confirmed by the evaluation of the scale of segregation, the concentration fields and the streamline plots. Only the hexahedron-dominated meshes show instationary flow patterns. The solution of the layered meshes for velocity, pressure and species concentration enter a stationary state. Lowering the tolerances of the solvers does prevent this but has no impact on the results.

- The global Sherwood numbers of the hexahedron-dominated meshes differ qualitatively and quantitatively from each other. Setups with $1.6 \cdot 10^6$, $3.2 \cdot 10^6$, $4.1 \cdot 10^6$ and $5.0 \cdot 10^6$ cells are tested.

- The concentration fields and streamline plots of the layered and the polyhedra meshes show a closed wake without instabilities. The equivalent evaluation of the hexahedron-dominated meshes shows a three-dimensional instationary wake.

- All results are still mesh sensitive although the boundary layer cells in the polyhedra mesh are of the estimated size. This suggests that the correlation from chapter 1 overestimates the actual boundary layer size or that the influence of the wake resolution on the solution is underestimated.

- The influence of the size of the refinement region on the global Sherwood number is studied by varying the cylinder radius in the *medium* hexahedron-dominated mesh from 1.5 mm to 4 mm. The influence is neglectable. However, in setups with more cells this might be different, as the wake in the other hexahedron-dominated meshes has a different shape.

- The mesh of the layered and the polyhedra meshes is very uniform around the bubble. This could be jointly responsible for the observation that the results in these meshes show no instabilities. The quality of the shape representation can be decisive for the resolution of the hydrodynamics. The influence of a four times finer surface mesh on the results of the hexahedron-dominated meshes is studied. The change of results reduces between the *coarse* and the *fine* mesh.

- Setups with $Re = 50$ and $Sc = 10$ are calculated using the *fine* hexahedron-dominated mesh. The wake structure for $Re = 50$ is still instationary.

- The time performance is evaluated by means of the *medium* meshes with 400 000 cells. Independent from the number of processors, the layered mesh with polygonal base is the fastest, followed by the layered mesh with quadrilateral base, the hexahedron-dominated mesh and the polyhedra mesh. Influence factors are the communication effort between the processors, the number of iterations per solution, the average number of faces per cell and the decomposition process. Scaling between run-time and number of processors is evaluated by comparing the run-time with one processor to the results with two, four and eight processors:

  Layered mesh with quadrilateral base: 63 %, 26 % and 17 %;

  Hexahedron-dominated mesh: 57 %, 22 % and 14 %;

  Layered mesh with polygonal base: 60 %, 28 % and 17 %;

  Polyhedra mesh: 58 %, 26 % and 15 %.

  For all four meshing strategies the CPU-time with four processors is lower than with two processors and in the case of the hexahedron-dominated mesh even lower than with only one processor.

6.2 Best Practice Guide

In the following, some experiences and recommendations are compiled as a guidance for future studies.

- As a starting point, the concentration boundary layer thickness may be estimated as $\delta_c = d_b \cdot \sqrt{\pi}/(2 \cdot Pe)$.

- In `blockMesh` the number of cells in tangential direction can be adjusted, such that the surface in areas with high curvature can be represented better.

- Increasing the refinement region level in the hexahedron-dominated meshes approximately octuples the mesh size. Adjusting the mesh size in smaller steps can be achieved by changing the background mesh. A way to reduce the layer cell thickness without the drawback of a much larger mesh is increasing the surface refinement level.

- Reducing the final layer thickness or increasing the aspect ratio of a good hexahedron-dominated mesh can both lead to the problem of incomplete layer addition. Increasing the aspect ratio can require raising the final layer thickness.

- The mesh size of the layered meshes with polygonal base is much more sensitive to the edge length of the surface mesh. With the number of cells in radial direction the adjustment of the mesh size is more predictable and precise. This makes it difficult to keep the aspect ratio of the cells constant between two differently sized layered meshes with polygonal base.

- Adjusting the mesh size of the layered meshes by changing the cell sizes first and then increasing the aspect ratio as long as the mesh quality is acceptable can be a starting point for the production of good meshes.
- The development of the size in a polyhedra mesh is found to be more predictable when adjusting the mesh size of the surface mesh. Changing the approximate edge length in the volume mesh has a volatile influence on the mesh size.
- Refinement regions in the wake of the bubble can only be added in the hexahedron-dominated meshes and the polyhedra meshes, but not in the layered meshes.
- Hexahedron-dominated meshes are the most appropriate to achieve low non-orthogonalities. Layered meshes with polygonal base are the least convenient for this purpose.
- In terms of skewness, layered and hexahedron-dominated meshes are to be preferred over polyhedra meshes.
- Changing the mesh size without changing the approximate shape of the cells leads to comparable values for non-orthogonality and skewness.
- The concentration fields in the hexahedron-dominated meshes suggest that the refinement area should at least have the length of the bubble's semi-major axis as radius.
- Higher average numbers of faces per cell and of iterations per solution have a negative influence on the time performance. The number of processors influences the number of iterations. The layered meshes show to have an advantage in terms of run-time compared to the hexahedron-dominated and the polyhedra meshes.

6.3 Outlook

In the present work, chemical reactions between the transfer species and the bulk species were neglected to reduce complexity. In future studies, reactions such as single, decay, parallel competitive and parallel consecutive reactions could be considered.
With increasing mesh sizes, reducing the cell number by downsizing the refinement regions or raising the refinement level of the surface, for example, will become more important. Moreover, the influence of the parallelization increases with cell number and run-time. Therefore, the scaling of run-time and number of processors has to be investigated for finer meshes.
Because the resolution of the hydrodynamics is still mesh dependent, the adaption of the meshes to setups with lower Reynolds number is not sensible yet. The same applies to the effects of varying aspect ratios. An evaluation of the results for the hexahedron-dominated meshes with layers at the outer domain boundary is expected to bring better results. Additionally, an adjustment of the meshes to different Peclet numbers could be necessary. The boundary layer thicknesses calculated with potential flow theory are only an estimation, and it turns out that in some cases the boundary layer is thicker or thinner than expected.

Bibliography

[1] D. Bothe, C. Stemich, and H.-J. Warnecke. Theoretische und experimentelle Untersuchungen der Mischvorgänge in T-förmigen Mikroreaktoren – Teil 1: Numerische Simulation und Beurteilung des Strömungsmischens. *Chemie Ingenieur Technik*, 76(10):1480–1484, 2004.

[2] D. Bothe and H.-J. Warnecke. Berechnung und Beurteilung strömungsbasierter komplex-laminarer Mischprozesse. *Chemie Ingenieur Technik*, 79(7):1001–1014, 2007.

[3] A. Ferreira, P. Cardoso, J. Teixeira, and F. Rocha. PH influence on oxygen mass transfer coefficient in a bubble column. Individual characterization of kl and a. *Chemical Engineering Science*, 100:145 – 152, 2013. 11th International Conference on Gas-Liquid and Gas-Liquid-Solid Reactor Engineering.

[4] B. Figueroa-Espinoza and D. Legendre. Mass or heat transfer from spheroidal gas bubbles rising through a stationary liquid. *Chemical Engineering Science*, 65(23):6296 – 6309, 2010.

[5] J. R. G. R. Clift and M. E. Weber. *Bubbles, Drops and Particles*. Academic Press, 1978.

[6] A. Weiner and D. Bothe. Advanced subgrid-scale modeling for convection-dominated species transport at fluid interfaces with application to mass transfer from rising bubbles. *Journal of Computational Physics*, 347:261 – 289, 2017.